J. Fluid Mech. (1992), *vol.* 240, *pp.* 59–96
Printed in Great Britain

A new modelling of cavitating flows: a numerical study of unsteady cavitation on a hydrofoil section

By AKIHIRO KUBOTA, HIROHARU KATO
AND HAJIME YAMAGUCHI

Department of Naval Architecture and Ocean Engineering, Faculty of Engineering,
The University of Tokyo, 7-3-1 Hongo, Bunkyo-ku, Tokyo 113, Japan

(Received 22 March 1990 and in revised form 27 November 1991)

A new cavity model that can explain the interaction between viscous effects including vortices and cavitation bubbles is presented in this study. This model, which is named a bubble two-phase flow (BTF) model, treats the inside and outside of a cavity as one continuum by regarding the cavity as a compressible viscous fluid whose density changes greatly. Navier–Stokes equations including cavitation bubble clusters are solved in finite-difference form by a time-marching scheme, where the growth and collapse of a bubble cluster is given by a modified Rayleigh's equation. Computation was made on a two-dimensional flow field around a hydrofoil NACA0015 at angles of attack of 8° and 20°. The Reynolds number was 3×10^5. The experiments were also performed at the same Reynolds number for comparison. The computed results by the BTF cavity model can express the feature of cloud-type cavitation shed from the trailing edge of the attached cavities when the angle of attack is 8°. It shows the mechanism of cavitation cloud generation and large-scale vortices. The boundary layer separates at the cavity leading edge. Then it rolls up and produces the cavitation cloud. In other words, the instability of the shear layer may produce the cavitation cloud. When the angle of attack is 20°, the flow was fully separated from the leading edge of the hydrofoil and vortex cavitation occurs in the separated region. The BTF cavity model can also express the generation of such vortex cavitation and the effect of cavitation nuclei in the uniform flow.

1. Introduction

Cavitation (Knapp, Daily & Hammit 1970) is a very complex vapour–liquid two-phase flow including phase changes and viscous effects. In spite of many excellent studies, the actual structure of cavitation is not yet fully understood.

Vortex cavitation is often observed downstream of attached cavitation. It is caused by vorticity shed into the flow field just downstream of the cavity. Such vortex cavitation generates a large cavitation cloud under certain conditions. The vortex cavitation impinges on the body where its subsequent collapse results in erosion (Hutton 1986). In a previous work, the authors performed an experimental investigation of the unsteady structure (velocity distribution) of cloud cavitation on a stationary two-dimensional hydrofoil using a conditional sampling technique (Kubota *et al.* 1989*a*). It was found that the cloud cavitation observed in the experiment was a large-scale vortex with many small cavitation bubbles. Consequently, the importance of the interaction between large-scale coherent vortices in the flow field and cavitation bubbles was recognized.

Much theoretical work has also been done in order to obtain a better understanding of the physics of the cavitation phenomenon. Researchers have continually developed new models of cavitating flow based mainly on the assumption that the flow is irrotational (inviscid). Helmholtz (1868) and Kirchhoff (1869) proposed nonlinear theory using hodograph mapping. Tulin (1955, 1964) proposed small-perturbation (linearized) theory for the case of a supercavitating hydrofoil. They have treated the cavity as a single vapour film and assumed that the pressure inside the cavity is constant. This is a sort of macroscopic analysis of cavitation. Using this modelling, many researchers have gradually improved the calculation methods. For example, Wu (1962) solved fully as well as partially cavitating hydrofoils using conformal transformation. Nishiyama & Miyamoto (1969) treated the problem of a supercavitating foil placed under a free surface by a singularity method. Furuya also solved a three-dimensional supercavitating hydrofoil near a free surface (1975) and cavitating cascade (1980) including nonlinearity at the leading edge. Yamaguchi & Kato (1983) applied the singularity distribution method to a partially cavitating hydrofoil with an arbitrary profile in which the cavity does not occur at the leading edge of the hydrofoil. Recently, Lemonnier & Rowe (1988) modified their calculation method, which was based on the panel method, in order to reduce a discretization error as much as possible. All the above single vapour film models are now well established. These models can also predict macroscopic cavity characteristics fairly well. However, they all dealt with only steady cavitation. Furness & Hutton (1975) treated the case of an unsteady attached cavity on a stationary two-dimensional body by the singularity method. This calculation result showed unsteadiness of the cavity surface and a re-entrant jet (Knapp *et al.* 1970). Their methods, however, could not predict the behaviour of a detached cavity after attached cavitation splits into two parts. Tulin & Hsu (1980), and van Houten (1982) have solved the unsteady cavity problem on a stationary or periodically oscillating hydrofoil. Their method also could not predict the generation of detached cavitation clouds. This is because of a limitation of the cavity model, which treats the cavity as a single vapour film where pressure is constant. Therefore, a new model of cavitation is required to study theoretically the breakoffs of attached cavities and cavitation clouds.

How to model the cavity trailing edge, where the cavity collapses, is the most difficult problem for the above-mentioned single-film, constant-pressure cavity model. Up until now, the mirror-image model (Riabouchinsky 1920), the re-entrant jet model (Kreisel 1946; Efros 1946), the transient flow model (Wu 1962) and the spiral vortex model (Tulin 1964) have all been put forward. When one observes actual cavitation, it is found that the sheet cavity splits into minute bubbles with vortices in the end region. Then the bubbles collapse. One can often observe many vortex cavities in this region even if the sheet cavity is stable. Nevertheless, this method of vapour-film modelling cannot explain the mechanism of a single-vapour-film-type cavity splitting into tiny bubbles.

Van Wijngaarden (1964, 1968), Mørch (1981), Chahine & Lie (1985), d'Agostino & Brennen (1989) and others have studied the dynamics of bubble clusters. The bubble cluster is a kind of microscopic modelling of cavitation. However, these studies treated only a cluster of collapsing bubbles under given conditions. Hence, they could not answer the question of how the unsteady attached cavity sheds cavitation clouds.

Highly vortical fluid motion such as a cavitation cloud is often observed downstream of a cavity. Experimental observation shows a close relationship between large-scale coherent vortex and cavitation (Kubota *et al.* 1989*a*). Therefore, it is necessary to investigate the mechanism that generates the large-scale vortex structure. There is a strong interaction between the large-scale vortex and cavitation. The occurrence of attached cavitation yields boundary-layer separation. The separated shear layer rolls up, thus turning into a large-scale vortex (Kiya & Sasaki 1985). On the contrary, the large-scale vortex yields a low-pressure region at its centre. In the low-pressure region, bubbles grow and remain. Existing cavity models are powerless to explain the nonlinear interaction between cavitation bubbles and viscous phenomena.

In this paper, we propose a new cavity model that can express the interactions between vortices and bubbles. We call this new model a bubble two-phase flow (BTF) cavity model. In a macroscopic (coarse-grained) view, this model treats the cavity flow field phenomenologically as a compressible viscous fluid whose density varies greatly. Thus it treats the inside and outside of the cavitation as a single continuum. In a microscopic view, it treats cavitation structurally as bubble clusters. This is because the bubbles play an important role in the vortex cavitation. Consequently, the BTF model can express the nonlinear interaction between macroscopic vortex motion and microscopic bubble dynamics. In §2, we shall discuss the detailed concept of the BTF cavity model and formulate the model.

Section 3 presents a numerical solution method to solve the BTF cavity model formulated in §2. A finite-difference method is employed to solve the system of partial differential equations, including Navier–Stokes and Rayleigh's equations, given by the BTF cavity model. Over several years, the authors developed a program code SACT-II (solution algorithm for cavitation and turbulence, version II; two-dimensional rectangular cell version) (Kubota, Kato & Yamaguchi 1988). Now, the authors have developed a new program code called SACT-III. SACT-III can solve the BTF-cavity-model equations by a time-marching scheme in a three-dimensional boundary-fitted curvilinear coordinate system (Kubota *et al.* 1989*b*).

Section 4 will be devoted to the discussion of some computed results around a two-dimensional hydrofoil. Computations are performed both at high and low angles of attack in order to examine the validity and flexibility of the BTF cavity model and SACT-III. When the angle of attack is low, attached cavities which shed cavitation clouds cyclically occur at the leading edge of the hydrofoil. When the angle of attack is high, the flow around the hydrofoil is fully separated. Vortex cavitation occurs in the separated region.

Section 5 will describe the experimental results and compare them with the computational results presented in §4. The experiment was performed at the same Reynolds number as that used for the computation.

2. Formulation of the bubble two-phase flow cavity model

Figure 1 shows examples of the cavity appearance on a hydrofoil section. When the angle of attack is low, an attached cavity occurs from the leading edge of the hydrofoil. Then it collapses at the mid-portion of the hydrofoil. The attached cavity oscillates cyclically within a certain range of cavitation number. The unsteady cavity sheds a cavitation cloud in each cycle as shown in the above figure (Kubota *et al.* 1989*a*). The front part of the attached cavity is a film of vapour where pressure is constant. At its rear part, the vapour film splits up into tiny bubbles. A large-scale vortex caused by the cavity rolls up the bubbles, thus generating a cavitation cloud. The collapsing region of the cavitation cloud is important for investigating the generation mechanism of noise, vibration and erosion.

When the angle of attack is high, vortex cavitation occurs in the separated region

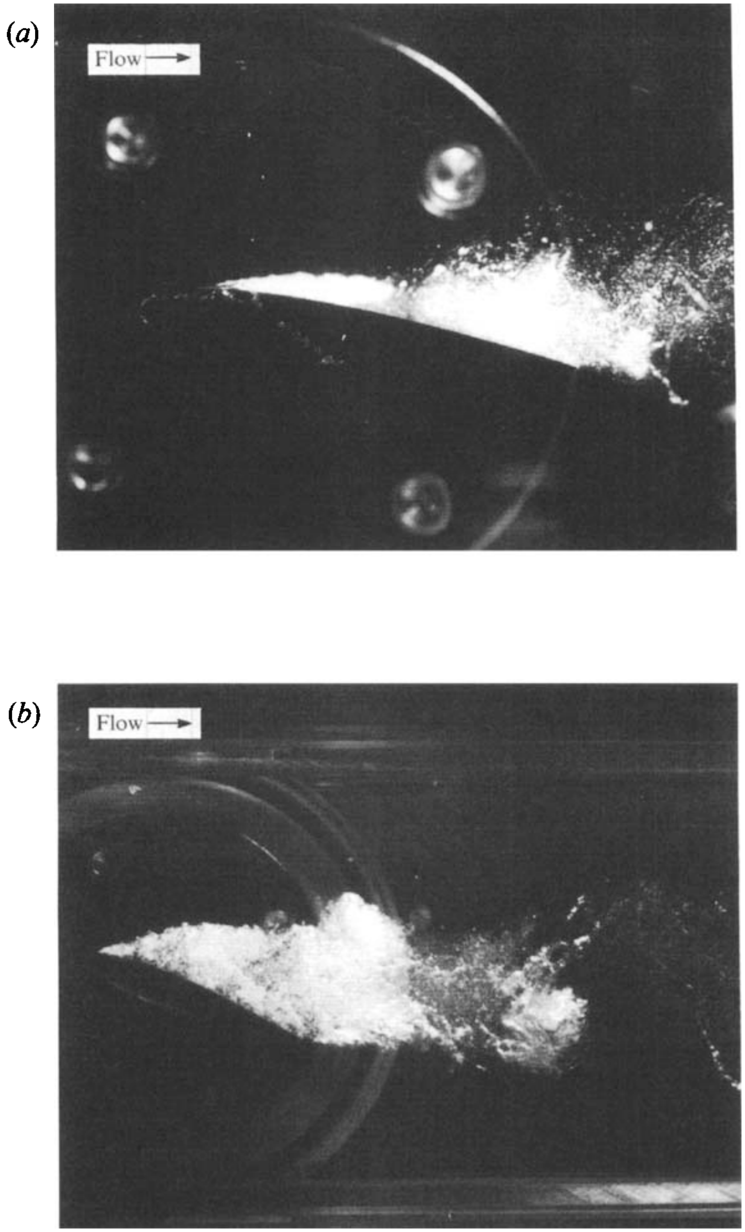

FIGURE 1. Unsteady cavitation on a hydrofoil, NACA0015; $Re = 3\times10^5$. (a) $\alpha = 8°$; (b) $\alpha = 20°$.

since the flow is fully separated from the foil leading edge. Both the cavitation cloud and the vortex cavitation consist of bubble clusters containing many small bubbles.

2.1. *Macroscopic modelling*

In the macroscopic view, the bubble two-phase flow model treats the inside and outside of the cavitation as one continuum. This is because it regards the cavity flow field as a compressible viscous fluid whose density varies greatly. According to this phenomenological modelling, contour lines of the void fraction (volume fraction of cavities) express the shape of cavity as shown in figure 2.

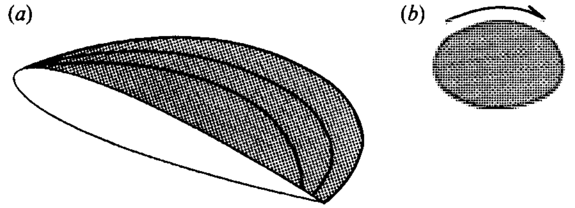

FIGURE 2. Modelling concept of bubble two-phase flow (BTF) cavity model. (*a*) Void fraction contours. (*b*) Cavitation cloud.

Governing equations of the macroscopic flow field are as shown below.

The equation of continuity is

$$\frac{\partial \rho}{\partial t}+\nabla\cdot(\rho \boldsymbol{v}) = 0, \tag{1}$$

where t, $\rho \boldsymbol{v}$, $\boldsymbol{v}$ and ρ are time, mass flux vector $(\rho u, \rho v, \rho w)$, velocity vector (u, v, w) and density of the mixture, respectively.

The conservation equation for momentum: Navier–Stokes equation is

$$\frac{\partial(\rho \boldsymbol{v})}{\partial t}+\nabla\cdot(\rho \boldsymbol{v}\boldsymbol{v}) = -\nabla P+\frac{1}{Re}\mu\{\nabla^2 \boldsymbol{v}+\tfrac{1}{3}\nabla(\nabla\cdot \boldsymbol{v})\}, \tag{2}$$

where P is the pressure in the mixture, μ is the viscosity of the mixture, and Re is the Reynolds number. This equation is in conservation form (Roache 1976). Liquid is treated as incompressible. Only the change of void fraction causes the compressibility of the mixture. It is assumed that there is no slip between the two phases. The non-dimensionalized quantities based on the uniform flow velocity and a reference length have been employed in the equations as shown later ((15) and (16)).

The BTF cavity model assumes that a fluid of variable density replaces the water–vapour mixture. The density of the water containing bubbles (mixture) is defined as follows:

$$\rho = (1-f_g)\rho_L, \tag{3}$$

where ρ_L is the water density and f_g is the local void fraction. The mass and momentum of the vapour are ignored, since they are very small compared with those of the liquid. The actual ratio of the density of vapour to that of liquid is of the order 10^{-4}. The change of liquid mass owing to the phase change is also ignored. The phase change only affects the change of void fraction (density) in the mixture.

The viscosity of the mixture is assumed to be,

$$\mu = (1-f_g)\mu_L+f_g\mu_G, \tag{4}$$

where μ_L is the water viscosity and μ_G is the vapour viscosity.

Equation (4) seems to be robust computationally. Nevertheless, the dissipation is very important for the highly bubbly churning flow (Taylor 1932). When the bubbles are small, it is said that the viscosity of the mixture increases in proportion to the void fraction. However, when the cavity contains many large bubbles and the void fraction approaches one, the viscosity should reduce to the vapour viscosity. It is still difficult to formulate the viscosity of a mixture whose density varies greatly. This is why this simple equation is used in this study.

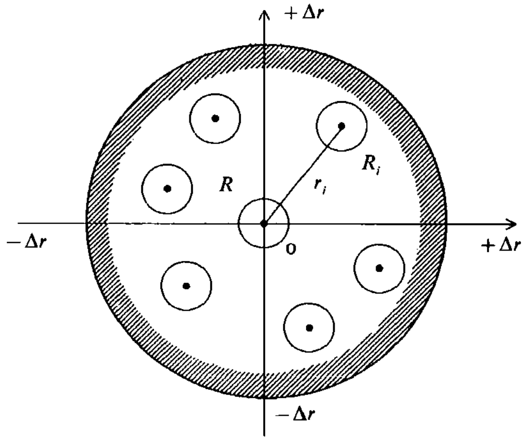

FIGURE 3. Sun-grid-scale (SGS) bubble interaction model.

2.2. *Microscopic modelling – local homogeneous model*

To calculate the macroscopic flow field, it is necessary to know the local void fraction function $f_g(t, x, y, z)$. The greatest problem is to develop a model that gives the relationship between the flow field condition and the void fraction. The present BTF model treats cavitation microscopically as bubble clusters. This is because one of the main purpose of the BTF model is to study the vortex cavitation containing many tiny bubbles. In this study, a local homogeneous model (LHM) is introduced for simplicity. This model is a sort of mean field approximation (MFA). It treats the cavity as a local homogeneous cluster of spherical bubbles. Bubble number density and a single typical radius are assumed locally. This typical bubble radius is obtained from the equation of the bubble cluster. However, this structural microscopic model cannot be applied to the vapour-film-type cavitation in its strict physical meaning.

The LHM gives the local void fraction f_g by coupling the bubble density and the typical bubble radius as follows:

$$f_g = n\tfrac{4}{3}\pi R^3 \quad (0 < f_g < 1), \tag{5}$$

where n is the bubble number density and R is the typical bubble radius.

The LHM assumes that the bubbles are spherical and that they remain separate and distant enough from each other.

In the present computation, the bubble density n is assumed to be constant all over the computational domain, though real cavity flows have a distributed bubble density. It is known that the rear part of the attached cavity is an abundant source of micro bubbles. However, it is too difficult to formulate coalescence and fragmentation of the bubbles.

Lord Rayleigh originally derived the equation of radial motion (growth and collapse) of an isolated spherical bubble in a homogeneous infinite medium (Lamb 1932). This equation is widely known as Rayleigh's equation. It takes the following form, neglecting the effect of surface tension and viscous damping,

$$R\frac{\mathrm{d}^2R}{\mathrm{d}t^2}+\frac{3}{2}\left(\frac{\mathrm{d}R}{\mathrm{d}t}\right)^2=\frac{P_\mathrm{v}-P}{\rho_\mathrm{L}}, \tag{6}$$

where P_v is the vapour pressure. In this study, the vapour pressure is assumed to be constant. This means the behaviour of the bubble is regarded as nearly isothermal and gas inside the bubble is also ignored.

As mentioned in §1, the finite-difference method was employed for the present SACT-III. In this method, a continuous domain is discretized into finite grid points. Hence, an interaction between individual bubbles within the grid spacing must be considered to eliminate the effect of the computational grid. This effect is a sub-grid-scale (SGS) bubble interaction. Next, let us consider the SGS bubble interaction of the LHM, deriving analytically the equation of motion of the bubble cluster.

As shown in figure 3, we consider the influence of the other bubbles which exist inside the distance r which corresponds to the grid spacing. The total velocity potential due to the other bubbles at the origin O is

$$\sum^{i} \frac{1}{r_i}\frac{dR_i}{\mathrm{d}t}R_i^2, \tag{7}$$

when $R_i \ll r_i$. The relative position of the bubbles is assumed to be unchanging. From the local homogeneous assumption,

$$\nabla\left(\sum^{i} \frac{1}{r_i}\frac{dR_i}{\mathrm{d}t}R_i^2\right) = 0, \tag{8}$$

and

$$R_i = R. \tag{9}$$

The following equation is therefore obtained by adding the time derivative of (7) to the original equation (6):

$$\frac{\mathrm{d}}{\mathrm{d}t}\left(\sum^{i} \frac{1}{r_i}\frac{\mathrm{d}R}{\mathrm{d}t}R^2\right) + R\frac{\mathrm{d}^2R}{\mathrm{d}t^2} + \frac{3}{2}\left(\frac{\mathrm{d}R}{\mathrm{d}t}\right)^2 = \frac{P_\mathrm{v}-P}{\rho_\mathrm{L}}. \tag{10}$$

The number of bubbles inside the sphere of radius Δr is

$$n\tfrac{4}{3}\pi\Delta r^3. \tag{11}$$

Then the first term of the left-hand side in (10) becomes

$$\begin{aligned}\frac{\mathrm{d}}{\mathrm{d}t}\left(\sum^{i} \frac{1}{r_i}\frac{\mathrm{d}R}{\mathrm{d}t}R^2\right) &= \frac{\mathrm{d}}{\mathrm{d}t}\left(\frac{\mathrm{d}R}{\mathrm{d}t}R^2\sum^{i}\frac{1}{r_i}\right)\\ &\approx \frac{\mathrm{d}}{\mathrm{d}t}\left(\frac{\mathrm{d}R}{\mathrm{d}t}R^2 n\int_0^{\Delta r}\frac{1}{r}4\pi r^2\,\mathrm{d}r\right)\\ &= \frac{\mathrm{d}}{\mathrm{d}t}\left(\frac{\mathrm{d}R}{\mathrm{d}t}R^2 n 2\pi\Delta r^2\right)\\ &= 2\pi\Delta r^2\left[nR^2\frac{\mathrm{d}^2R}{\mathrm{d}t^2} + \frac{\mathrm{d}n}{\mathrm{d}t}R^2\frac{\mathrm{d}R}{\mathrm{d}t} + 2nR\left(\frac{\mathrm{d}R}{\mathrm{d}t}\right)^2\right].\end{aligned} \tag{12}$$

Combining (10) with (12), the following equation is obtained:

$$(1+2\pi\Delta r^2 nR)R\frac{\mathrm{d}^2R}{\mathrm{d}t^2} + (\tfrac{3}{2}+4\pi\Delta r^2 nR)\left(\frac{\mathrm{d}R}{\mathrm{d}t}\right)^2 + 2\pi\Delta r^2\frac{\mathrm{d}n}{\mathrm{d}t}R^2\frac{\mathrm{d}R}{\mathrm{d}t} = \frac{P_\mathrm{v}-P}{\rho_\mathrm{L}}. \tag{13}$$

The slip between bubbles and liquid is not taken into account, i.e. it is assumed that the bubbles are convected with the same velocity as liquid. The time derivative $\mathrm{d}/\mathrm{d}t$ is therefore replaced by

$$\frac{\mathrm{D}}{\mathrm{D}t}\left\{\equiv\frac{\partial}{\partial t}+(\boldsymbol{v}\cdot\nabla)\right\}.$$

Thus we obtain the LHM equation of motion as follows:

$$(1+2\pi\Delta r^2 nR)\,R\frac{\mathrm{D}^2R}{\mathrm{D}t^2}+(\tfrac{3}{2}+4\pi\Delta r^2 nR)\left(\frac{\mathrm{D}R}{\mathrm{D}t}\right)^2+2\pi\Delta r^2\frac{\mathrm{D}n}{\mathrm{D}t}R^2\frac{\mathrm{D}R}{\mathrm{D}t}=\frac{P_{\mathrm{v}}-P}{\rho_{\mathrm{L}}}. \qquad (14)$$

According to (14), the effect of the other bubbles decreases with the grid interval Δr. This is useful in solving the present problem. This behaviour is similar to Smagorinsky's SGS turbulence model (Smagorinsky 1963).

Quantities in the above equations have been non-dimensionalized based on the uniform flow velocity U^*_∞ and a reference length d^*. Hence:

$$\left.\begin{array}{lll} P^*=\rho^*_{\mathrm{L}}U^{*\,2}_\infty P, & t^*=td^*/U^*_\infty, & \\ V^*=U^*_\infty V, & & \\ \rho^*=\rho^*_{\mathrm{L}}\rho, & \mu^*=\mu^*_{\mathrm{L}}\mu, & \\ n^*=n/d^{*3}, & R^*=d^*R, & \\ x^*=d^*x, & y^*=d^*y, & z^*=d^*z, \end{array}\right\} \qquad (15)$$

where * denotes dimensional values. In the following computation, the chord length of a hydrofoil has been chosen as d^*. The Reynolds number Re, pressure coefficient C_p and cavitation number σ are defined as follows:

$$\left.\begin{array}{l} Re=U^*_\infty d^*/\nu^*_{\mathrm{L}}=U^*_\infty d^*\rho^*_{\mathrm{L}}/\mu^*_{\mathrm{L}}, \\ C_p=(P^*-P^*_\infty)/(0.5\rho^*_{\mathrm{L}}U^{*2}_\infty)=2(P-P_\infty), \\ \sigma=(P^*_\infty-P^*_{\mathrm{v}})/(0.5\rho^*_{\mathrm{L}}U^{*2}_\infty)=2(P_\infty-P_{\mathrm{v}}). \end{array}\right\} \qquad (16)$$

3. SACT-III program

The SACT-III program is the third version of the SACT (Solution Algorithm for Cavitation and Turbulence) series (Kubota *et al.* 1988, 1989*b*). The finite difference method is employed in the body fitted coordinates to solve the governing partial differential equations given in the preceding section. This section explains the computational procedure and the finite difference scheme of the SACT-III. The computational procedure is basically parallel with the Marker-and-Cell (MAC) method (Harlow and Welch, 1965) except for the use of a regular mesh system.

3.1. *Quasi-Poisson equation for pressure*

By taking the divergence of the Navier–Stokes equation (2), the following Poisson equation for pressure is given:

$$\begin{aligned} \nabla^2P &= -\nabla\left(\frac{\partial(\rho\boldsymbol{v})}{\partial t}\right)+\mathscr{D}(\rho\boldsymbol{v},\boldsymbol{v}) \\ &= -\frac{\partial}{\partial t}\{\nabla(\rho\boldsymbol{v})\}+\mathscr{D}(\rho\boldsymbol{v},\boldsymbol{v}), \end{aligned} \qquad (17)$$

where

$$\mathscr{D}(\rho\boldsymbol{v},\boldsymbol{v})=-\nabla\left[\nabla\cdot(\rho\boldsymbol{v}\boldsymbol{v})-\frac{1}{Re}\mu\{\nabla^2\boldsymbol{v}+\tfrac{1}{3}\nabla(\nabla\cdot\boldsymbol{v})\}\right]. \qquad (18)$$

Substituting the continuity equation (1) into (18),

$$\nabla^2P=\frac{\partial^2\rho}{\partial t^2}+\mathscr{D}(\rho\boldsymbol{v},\boldsymbol{v}). \qquad (19)$$

From (3) and (5),

$$\rho=(1-n\tfrac{4}{3}\pi R^3)\,\rho_{\mathrm{L}}. \qquad (20)$$

By differentiating equation (20) twice by t, we have the following equation:

$$\frac{\partial^2 \rho}{\partial t^2} = -\rho_{\mathrm{L}} 4n\pi \left\{ R^2 \frac{\partial^2 R}{\partial t^2} + 2R \left(\frac{\partial R}{\partial t} \right)^2 \right\}, \tag{21}$$

where n is assumed constant in this study, as mentioned in §2.

From (14),

$$\frac{\partial^2 R}{\partial t^2} = \mathscr{R}\left(\rho \boldsymbol{v}, \boldsymbol{v}, \frac{\partial R}{\partial t}, R\right) + \mathscr{P}(P), \tag{22}$$

where

$$\begin{aligned} \mathscr{R}\left(\rho \boldsymbol{v}, \boldsymbol{v}, \frac{\partial R}{\partial t}, R\right) = &-\left\{ 2(\boldsymbol{v}\cdot\boldsymbol{\nabla}) \frac{\partial R}{\partial t} + (\boldsymbol{v}\cdot\boldsymbol{\nabla})(\boldsymbol{v}\cdot\boldsymbol{\nabla}) R \right\} \\ &- \frac{\frac{3}{2} + 4\pi\Delta r^2 n R}{(1 + 2\pi\Delta r^2 n R) R} \left\{ \frac{\partial R}{\partial t} + (\boldsymbol{v}\cdot\boldsymbol{\nabla}) R \right\}^2 \\ &- \frac{2\pi\Delta r^2 R}{(1 + 2\pi\Delta r^2 n R) R} \left\{ \frac{\partial n}{\partial t} + (\boldsymbol{v}\cdot\boldsymbol{\nabla}) n \right\} \left\{ \frac{\partial R}{\partial t} + (\boldsymbol{v}\cdot\boldsymbol{\nabla}) R \right\} \end{aligned} \tag{23}$$

and

$$\mathscr{P}(P) = \frac{P_{\mathrm{v}} - P}{(1 + 2\pi\Delta r^2 n R) R \rho_{\mathrm{L}}}. \tag{24}$$

If $n = \text{constant}$, the last term of the right-hand side becomes zero in (23). Substituting (21) and (22) into (19), we obtain the quasi-Poisson equation for pressure including the motion of the cluster bubbles as follows:

$$\boldsymbol{\nabla}^2 P + \mathscr{P}'(P) = \mathscr{R}'\left(\rho \boldsymbol{v}, \boldsymbol{v}, \frac{\partial R}{\partial t}, R\right) + \mathscr{D}(\rho \boldsymbol{v}, \boldsymbol{v}), \tag{25}$$

where

$$\mathscr{P}'(P) = -\rho_{\mathrm{L}} 4n\pi R^2 \mathscr{P}(P), \tag{26}$$

$$\mathscr{R}'\left(\rho \boldsymbol{v}, \boldsymbol{v}, \frac{\partial R}{\partial t}, R\right) = -\rho_{\mathrm{L}} 4n\pi R \left\{ R \mathscr{R}\left(\rho \boldsymbol{v}, \boldsymbol{v}, \frac{\partial R}{\partial t}, R\right) + 2\left(\frac{\partial R}{\partial t}\right)^2 \right\}. \tag{27}$$

The left-hand side in (25) is approximated by the second-order finite differencing scheme. As a consequence, linear simultaneous equations of pressure P are obtained if the right-hand side is given in (25). The SACT-III solves these simultaneous equations with a point successive relaxation method. Equation (25) is equivalent to the normal MAC method's Poisson equation of incompressible flow (Harlow & Welch 1965) when

$$\mathscr{P}' = \mathscr{R}' = 0.$$

They were always set at zero for non-cavitating conditions. If the mixture is filled with liquid, (14) cannot be solved since the bubble radius R becomes zero. If the mixture is filled with vapour, (2) cannot be solved since density of the mixture becomes zero. Hence, when the void fraction f_{g} was less than $f_{\mathrm{gmin}} (> 0.0)$ or more than $f_{\mathrm{gmax}} (< 1.0)$, the bubble radius was fixed. Then, $\mathscr{P}'$ and $\mathscr{R}'$ were also set at zero. In the following computations, f_{gmin} and f_{gmax} are set as follows:

$$f_{\mathrm{gmin}} = n \tfrac{4}{3} \pi R_0^3, \quad f_{\mathrm{gmax}} = 0.95,$$

where R_0 is an initial bubble radius.

3.2. *Numerical methods*

Equations (2) and (14) are time-integrated with the Euler explicit scheme using the value of pressure P obtained by solving (25). To solve a high-Reynolds-number flow, we must pay great attention to the differencing scheme of the nonlinear convective term $\nabla(\rho \boldsymbol{v}\boldsymbol{v})$ (Roache 1976). In this study, each nonlinear term in (2), for example $(\partial/\partial x)(\rho uv)$, was approximated with the fourth-order centred finite-differencing scheme with the fourth-derivative term:

$$0.5|u|\frac{\partial^4}{\partial x^4}(\rho v)\,\Delta x^3. \tag{28}$$

The fourth-derivative term plays an important role in stabilizing the calculation. Physically, the fourth-derivative term gives shorter-range diffusion compared with the second-derivative viscous term (Kawamura & Kuwahara 1984). The fourth-derivative term consequently stabilizes the computation without introducing any turbulent models. The universal applicability of the fourth-derivative term on the turbulent flow calculation is not yet certain. However, SACT-III introduces no turbulent model since there is no reliable one for the cavity bubble two-phase flow as treated here.

All the other space differential terms in (2) and (4) are approximated with the second-order centred differencing scheme. Equation (14), however, has no spatial diffusive term for bubble radius R and its time-derivative. The second-derivative term is accordingly added in (14) to eliminate the instability of the nonlinear terms. For example,

$$|u|\frac{\partial^2 R}{\partial x^2}\Delta x \tag{29}$$

is added into $u(\partial R/\partial x)$. This term means diffusion. It is the same magnitude as that of the ordinary first-order upwind scheme (Roache 1976).

To compute the high-Reynolds-number flow around a body of arbitrary shape, it is also convenient to use body-fitted coordinates through coordinate transformation. Figure 4 shows the grid system for the present problem of a flow around a two-dimensional hydrofoil. This system is called a C-type grid (Thompson, Warsi & Mastin 1985). The connected physical (x, y, z) domain around the hydrofoil is mapped onto the rectangular computational (ξ, η, ζ) domain. Here the pair of planes forming the branch cut are both on the same plane of the transformed region. The surface of the body is also mapped on the same plane as the branch cut.

A regular mesh system is employed. Velocities, pressure, bubble radius and its time derivative are given on the grid points. As shown in figure 4, the uniform flow boundary conditions are imposed at the outer-flow boundary. Those are:

$$u = 1, \quad v = w = 0, \quad \frac{\partial u}{\partial \eta} = \frac{\partial v}{\partial \eta} = \frac{\partial w}{\partial \eta} = 0, \quad R = R_0, \quad P = 0. \tag{30}$$

At the downstream and side boundaries, the boundary conditions of the zeroth order (zero-gradient) extrapolation are imposed. At the branch cut boundaries, the periodic boundary conditions are imposed. At the wall boundary, the following boundary conditions are imposed.

$$u = v = w = 0, \quad \frac{\partial P}{\partial \eta} = 0, \quad \frac{\partial R}{\partial \eta} = 0. \tag{31}$$

The zero normal pressure gradient boundary conditions are simple and stable. They are the same as the boundary-layer approximation for incompressible flow, but only approximately so when the flow is viscid and compressible (Roache 1976). However, their error is quite small when the computational grid is fine enough near the wall

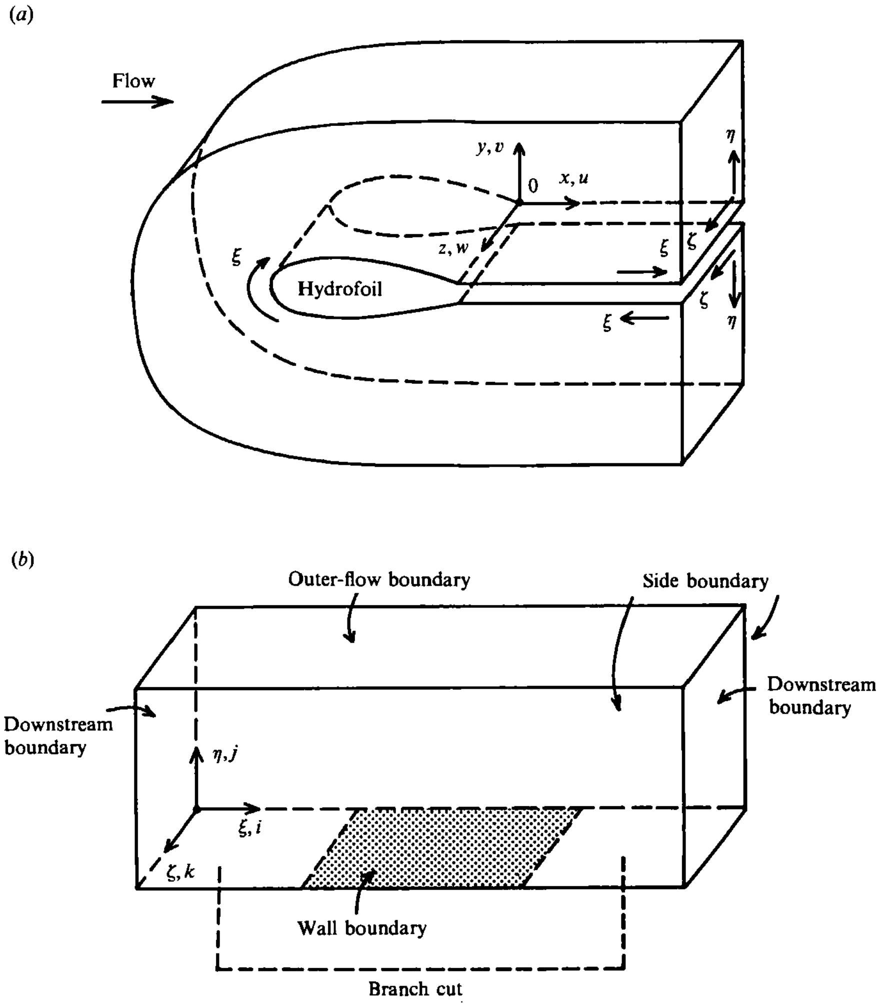

FIGURE 4. C-grid system around a two-dimensional hydrofoil. (*a*) Physical domain. (*b*) Transformed domain.

boundaries. The same boundary condition is also imposed for the bubble radius R according to the zero normal pressure gradient approximation. First-order (linear) extrapolation is used in the (ξ, η, ζ) domain for the velocities to calculate the nonlinear terms, which are approximated by the fourth-order centred differencing scheme with the fourth-derivative term, in (2).

Initial conditions are as follows,

$$u = v = w = 0, \quad p = 0, \quad R = R_0.$$

4. Computational results and discussion

4.1. *Condition of computation*

A hydrofoil section with a simple mathematical configuration, NACA0015, was chosen for the computation (Abbott & von Doenhoff 1958). The computation was performed at angles of attack, α, of 0°, 8° and 20°. The Reynolds number Re, based

Foil section	NACA0015
Reynolds number Re	3×10^5
$\dfrac{\text{Vapour density } \rho_G}{\text{Water density } \rho_L}$	0
$\dfrac{\text{Vapour viscosity } \mu_G}{\text{Water viscosity } \mu_L}$	0.00912

Angle of attack α	0°	8°			20°		
Cavitation number α	no-cavity	no-cavity	1.2	1.0	no-cavity	1.0	2.0 1.0
Initial bubble radius R_0	—	—	4×10^{-4}	1×10^{-3}	—	4×10^{-4}	1×10^{-3}
Bubble number density n	—	—	1×10^{6}	1×10^{6}	—	1×10^{4}	1×10^{6}

TABLE 1. Computational conditions

on the uniform flow velocity and chord length of the hydrofoil, was 3×10^5 in all the computations. The computation at $\alpha = 0°$ was performed only for non-cavitating conditions to evaluate numerical accuracy. Experimental observation at $\alpha = 8°$ shows laminar separation without bursting near the leading edge. For cavitating conditions, an attached-type cavity and resulting cloud cavitation occur from the foil leading edge at low cavitation number. On the contrary, the flow is fully separated from the foil leading edge at $\alpha = 20°$, even for non-cavitating conditions. As the result, large-scale vortex cavitation occurs in the separated region. Table 1 denotes the computational conditions. As mentioned in §2.2, the bubble density is assumed to be constant all over the computational domain.

The time increment Δt was determined in each computational step to keep the Courant number less than 0.25. These low Courant numbers are needed to stabilize computations. The present computation is prone to instability since the density and pressure change widely. The relaxation factor was set to be 0.8 when (25) was solved with the successive relaxation method. However, it was reduced to 0.3 for cavitating conditions. The convergence condition of the pressure computation is as follows:

$$\max(|\Delta P|) < 0.001 \quad \text{(for non-cavitating conditions)},$$
$$\max(|\Delta P|) < 0.01 \quad \text{(for cavitating conditions)},$$

where ΔP is the residue of pressure in the iterative calculation.

Preceding the computations for cavitating conditions, it was necessary to evaluate the numerical accuracy of SACT-III for non-cavitating conditions. Figure 5 shows the C-grid system. The grids were uniform in the spanwise section. The number of grid points was 101 (ξ) × 31 (η) × 3 (ζ). The computations in this study were made on a two-dimensional flow field though the computer code was three-dimensional (Kubota *et al.* 1989*b*). The distance was 1.2 from the trailing edge to the upper or lower boundaries. It was the same as the distance of the experiments in §5. The distance was 3.0 between the trailing edge and the downstream boundary. The front-part shape of the outer-flow boundary was oval as shown in figure 5. A direct numerical method (Kodama 1988) was used for the grid generation. The minimum

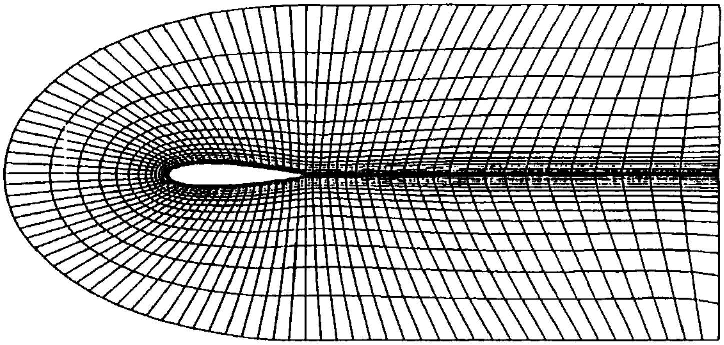

FIGURE 5. C-grid system around NACA0015 hydrofoil at $\alpha = 0°$, $101 \times 31 \times 3$.

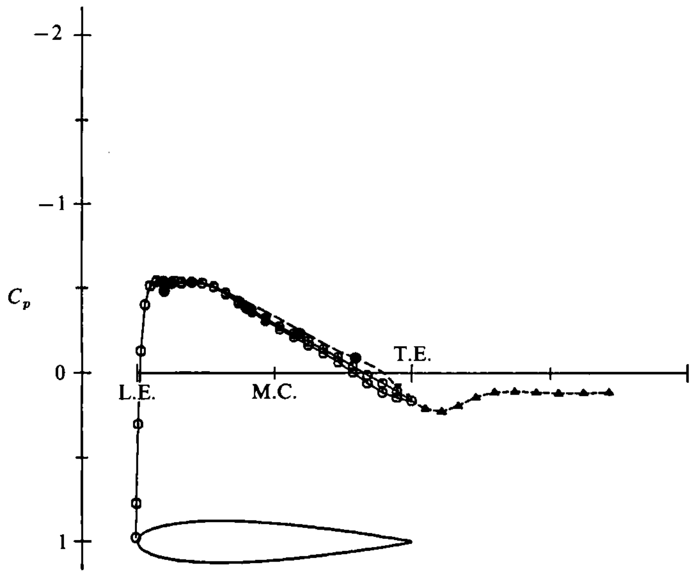

FIGURE 6. Foil surface and wake pressure coefficients, NACA0015, $\alpha = 0°$, $T = 2$: ●, experiment ($Re = 6 \times 10^5$); ○, △, present calculation ($Re = 3 \times 10^5$); ---, Hess–Smith method + boundary-layer calculation ($Re = 3 \times 10^5$).

grid spacings at the leading and trailing edges were 0.70×10^{-4} and 1.54×10^{-4}, respectively. The minimum spacing was about one twelfth of $Re^{-\frac{1}{2}}$ at the trailing edge.

Figure 6 shows the pressure distribution on the foil surface at $T = 2$ (T means time t). The angle of attack is 0°. The circles show the distribution of C_p on the foil surface. Since NACA0015 is a symmetrical hydrofoil, pressure on the upper and lower surfaces would be same. A little difference near the trailing edge is due to the asymmetry (unsteadiness) of the flow field. The triangles show the distribution of C_p in the wake, i.e. along the branch cut shown in figure 5. The computational result is compared with the computation using the Hess–Smith method (Hess & Smith 1967) and the measurement at $Re = 6 \times 10^5$ by Izumida (1980). The Hess–Smith method is a numerical solution method of potential flow based on the singularity distribution method. The foil shape was modified by adding the computed displacement thickness of the foil surface boundary layer (Yamaguchi *et al.* 1988). The computed result by SACT-III agrees very well with the others as shown in figure 8. Furthermore, the

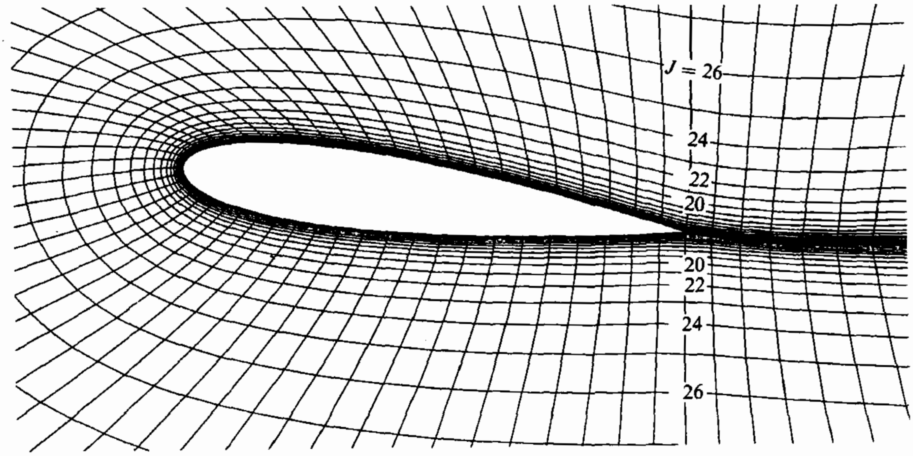

FIGURE 7. Close-up of the grid system around NACA0015 hydrofoil, $\alpha = 8°$, $101 \times 31 \times 3$.

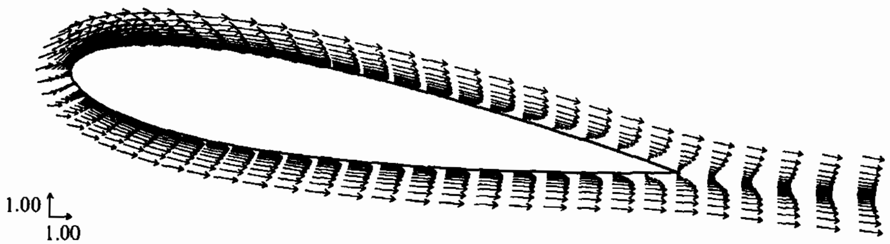

FIGURE 8. Computed velocity vectors around NACA0015 hydrofoil for non-cavitating conditions, $\alpha = 8°$, $Re = 3 \times 10^5$.

pressure coefficient at the front stagnation point is 0.982, which is almost equal to 1. As a consequence, the present numerical method has good accuracy when the grid system is fine enough. The computed pressure distributions disagree with the experimental result when the coarser grid systems near the foil surface are used (Kubota *et al.* 1989*b*).

4.2. *Structure of an unsteady attached cavity and its wake*

Figure 7 shows a close-up of the grid system around the NACA0015 hydrofoil. The angle of attack was 8°. The number of grid points was $101 \times 31 \times 3$. It was the same as that at $\alpha = 0°$. The minimum spacing was 0.7×10^{-4} at the trailing edge. It was almost the same as that of the grid system at $\alpha = 0°$. Figure 8 shows the time-averaged velocity vectors from $T = 2$ to 4 for non-cavitating conditions. The computation was performed stably. The main flow is from left to right. The boundary layer separates at $X = 0.74$ on the back. Instantaneous velocity vectors show unsteady vortex shedding from the foil trailing-edge region. In the other region, the flow is almost steady. No separation occurs near the leading edge.

Figure 9 shows the time-averaged pressure distribution on the foil surface and wake at $\alpha = 8°$. The result by SACT-III agrees fairly well with the experimental one. However, the computed C_p on the back is almost 0.3 higher than the experimental one. Prediction by the Hess–Smith method with the boundary-layer correction agrees very well with the experimental one. The lift coefficient C_L predicted by SACT-III is only about 58% of that obtained by experiment. Figures 10 and 11

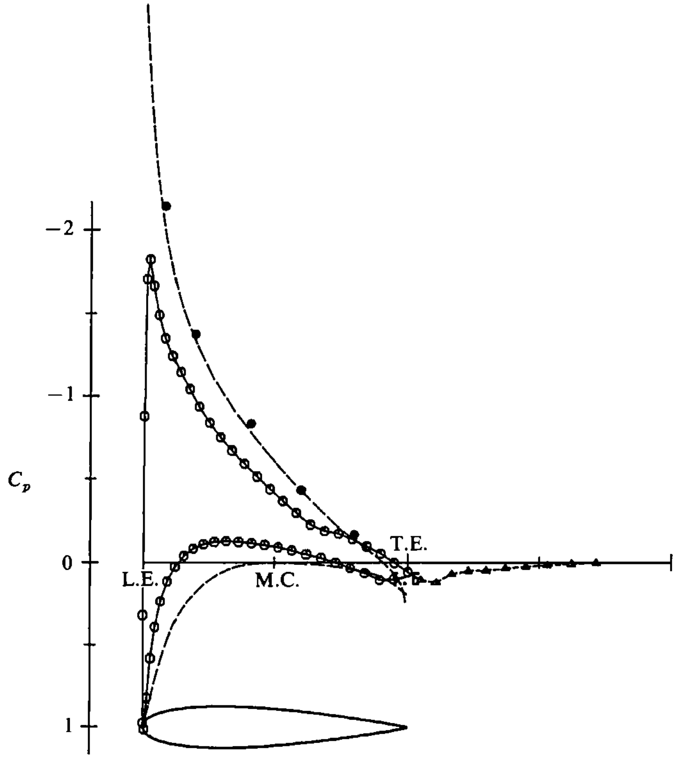

FIGURE 9. Time-averaged foil surface and wake pressure coefficients for non-cavitating conditions, NACA0015, $\alpha = 8°$, $Re = 3 \times 10^5$. ●, experiment; ○, △, present calculation; ---, Hess–Smith method + boundary layer calculation. C_L (experimental) = 0.946. C_L (calculated) = 0.5505.

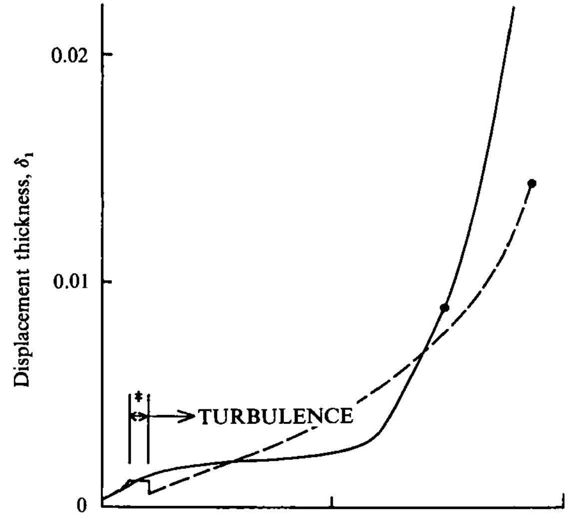

FIGURE 10. Boundary-layer displacement thickness distribution for non-cavitating conditions, NACA0015 back, $\alpha = 8°$, $Re = 3 \times 10^5$. ——, present calculation; ---, boundary-layer calculation; ●, separation point; *, separation bubble.

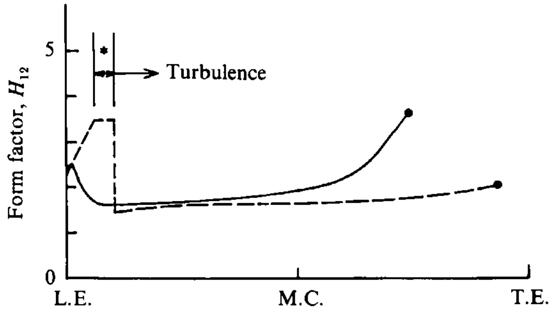

FIGURE 11. Boundary-layer form factor distribution for non-cavitating conditions, NACA0015 back, $\alpha = 8°$, $Re = 3\times10^5$. ——, present calculation; ---, boundary-layer calculation; ●, separation point; *, separation bubble.

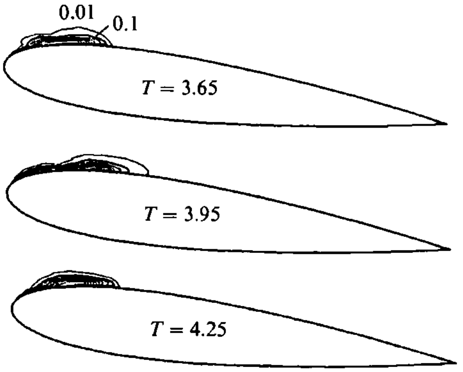

FIGURE 12. Void fraction contours around NACA0015 hydrofoil, $\sigma = 1.2$, $\alpha = 8°$, $Re = 3\times10^5$, the contour interval is 0.1 except for the most outer line.

shows the comparison of the boundary-layer-displacement thickness and form factor on the back between the present computation and the ordinary boundary-layer calculation. As shown in these figures, the boundary-layer characteristics agree well up to about 60% chord station. The disagreement of the pressure distribution must be because the trailing-edge separation occurs more upstream. However, the computed shape of the pressure distribution agrees well with the experiments. Hence, the disagreement of pressure hardly affects the nature of the unsteady cavitation (Kubota *et al.* 1989*b*).

In the following computation for cavitating conditions, the grid scale of the SGS bubble interaction model is assumed to be,

$$r = (g'/\pi)^{\frac{1}{2}}, \tag{32}$$

where $$g' = \frac{\partial x}{\partial \xi}\frac{\partial y}{\partial \eta} - \frac{\partial x}{\partial \eta}\frac{\partial y}{\partial \xi} \quad \text{(two-dimensional Jacobian).}$$

This is because the present computations are two-dimensional. Accordingly, the SGS bubble interaction effect is independent of the grid spacing in the spanwise direction.

Figure 12 shows contour lines of the void fraction at $\sigma = 1.2$. In this study, we define a cavity as a region where the void fraction is more than 0.1. The bold contour lines are those of $f_g = 0.1$ in this figure. Contour lines are drawn at an interval of 0.1

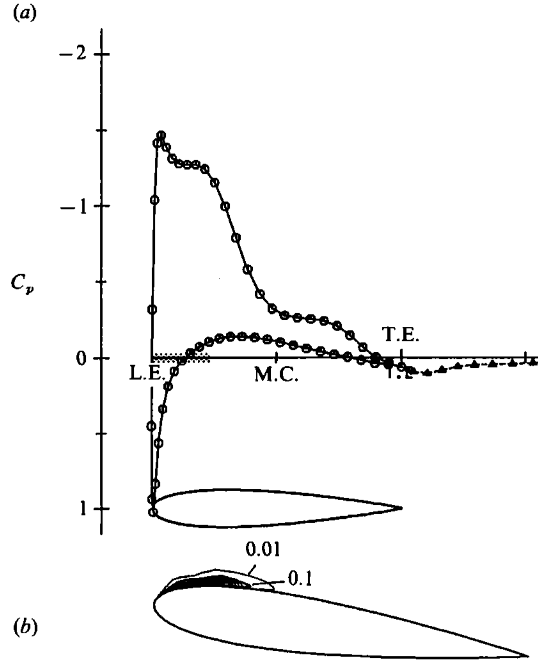

FIGURE 13. (*a*) Time-averaged pressure coefficient distribution and (*b*) void fraction contours around NACA0015 hydrofoil, $\sigma = 1.2$, $\alpha = 8°$, $Re = 3 \times 10^5$, the contour interval is 0.1 except for the most outer line. $T = 3\text{–}5$; $C_L = 0.5472$; $C_D = 0.0693$; ▨, cavity area.

except for the most outer line of $f_g = 0.01$. The rear portion of the cavity oscillates cyclically. Not only does the cavity length change, but the cavity also rises up at its rear part. The unsteady characteristics computed here agree well with the experimental observations of attached cavitation (Izumida *et al.* 1980).

Figure 13 shows the time-averaged pressure distribution on the foil surface and void fraction contour lines at $\sigma = 1.2$. The foil surface pressure where cavity exists is almost constant and equal to the vapour pressure ($C_p = -1.2$). However, a small negative pressure peak exists at the front of the cavity. Such pressure distribution is similar to the calculated result by a nonlinear free-stream line theory and the experimental ones (Yamaguchi & Kato 1982, 1983). Furthermore, the time-averaged cavity shape is similar with the experimental observation of attached cavity.

Figure 14 shows the close-up of time-averaged pressure contours around the hydrofoil at $\sigma = 1.2$. The contour line of $f_g = 0.1$ (the bold broken line) agrees approximately with that of $C_p = -1.2$. This is the reason why, in this study, the cavity is defined as a region where the void fraction is more than 0.1.

In the present computations, vorticity is defined as follows:

$$\omega = \frac{\partial y}{\partial y} - \frac{\partial v}{\partial x}. \tag{33}$$

The vorticity transport equation, which is obtained by taking curl of the momentum equation, for three-dimensional flow is written as:

$$\frac{D\omega}{Dt} = (\omega \cdot \nabla)\, v - (\nabla \cdot v)\, \omega + \frac{\nabla \rho \times \nabla P}{\rho^2}. \tag{34}$$

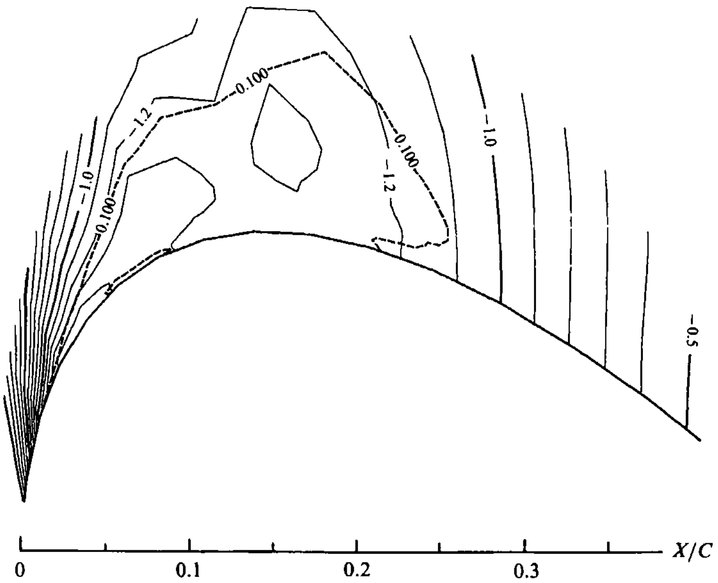

FIGURE 14. Close-up of time-averaged pressure coefficient contours, $\sigma = 1.2$, $\alpha = 8°$, $Re = 3 \times 10^5$, the contour interval is 0.1, the bold broken lines are void fraction contours of 0.1. Vertical exaggeration of 4 : 1.

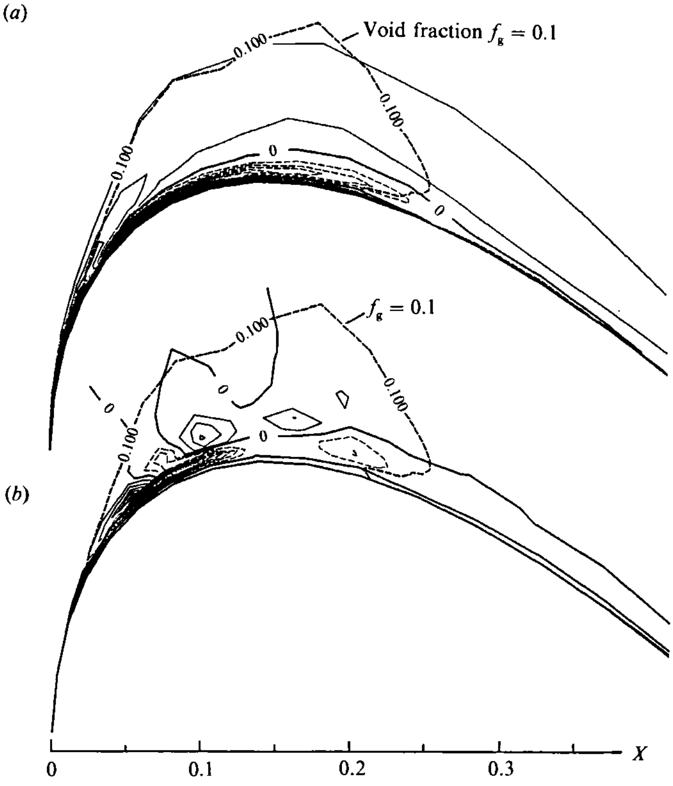

FIGURE 15. Close-ups of (*a*) vorticity contours (contour interval 50) and (*b*) baroclinic torque contours (contour interval 200), $\sigma = 1.2$, $\alpha = 8°$, $Re = 3 \times 10^5$, the bold broken lines are void fraction contours of 0.1. Vertical exaggeration of 4 : 1.

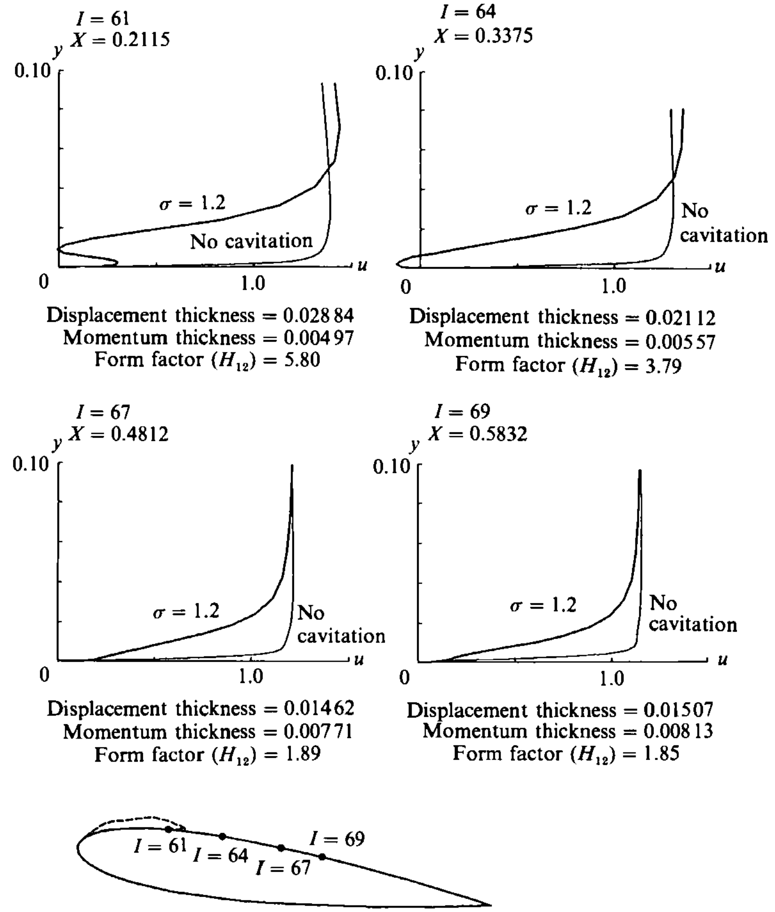

Displacement thickness = 0.028 84
Momentum thickness = 0.004 97
Form factor (H_{12}) = 5.80

Displacement thickness = 0.021 12
Momentum thickness = 0.005 57
Form factor (H_{12}) = 3.79

Displacement thickness = 0.014 62
Momentum thickness = 0.007 71
Form factor (H_{12}) = 1.89

Displacement thickness = 0.015 07
Momentum thickness = 0.008 13
Form factor (H_{12}) = 1.85

FIGURE 16. Time-averaged velocity profiles in cavity wake region, $\sigma = 1.2$, $\alpha = 8°$, $Re = 3 \times 10^5$, fine lines show the boundary-layer velocity profiles for non-cavitating conditions.

The viscous term is negligible since the Reynolds number of the flow is high. The left-hand term is the rate of change of vorticity by the fluid convection. The first term of the right-hand side is the vortex stretching. The second and the last terms are the fluid expansion and the baroclinic torque, respectively (Soetrisno *et al.* 1988). For two-dimensional flow, only the fluid expansion and the baroclinic torque are mechanisms for vorticity dynamics. The baroclinic torque is particularly important since it plays the role of source term of the vorticity caused by the density and pressure gradients. Figure 15 shows time-averaged contour lines of vorticity (positive in clockwise) and the baroclinic torque. Broken lines denote negative value in the vorticity and baroclinic torque contours. A large negative vorticity region exists in the cavity underlayer. The baroclinic torque also takes a large negative value there. It appears that the density change of fluid due to cavitation has a strong effect on vorticity dynamics.

Bold lines in figure 16 show time-averaged velocity profiles in the cavity wake boundary layer along η-coordinate. Fine ones are profiles for non-cavitating conditions. As shown in the section of $I = 61$ ($X = 0.2115$), the flow inside the cavity is quite slow except near the foil surface where a wall jet occurs. At the section of $I = 64$ ($X = 0.3375$), strong reverse flow occurs. At $I = 67$ and 69 ($X = 0.4812$ and

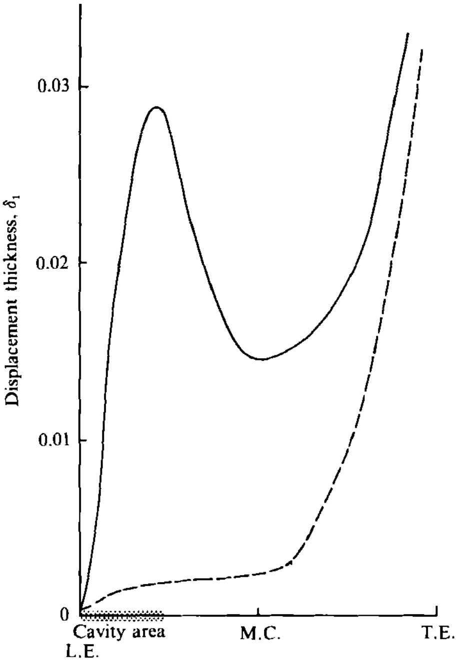

FIGURE 17. Comparison of boundary-layer displacement thickness distribution on the back of NACA0015 hydrofoil, $\sigma = 1.2$, $\alpha = 8°$, $Re = 3 \times 10^5$. ——, $\sigma = 1.2$; --- no cavitation.

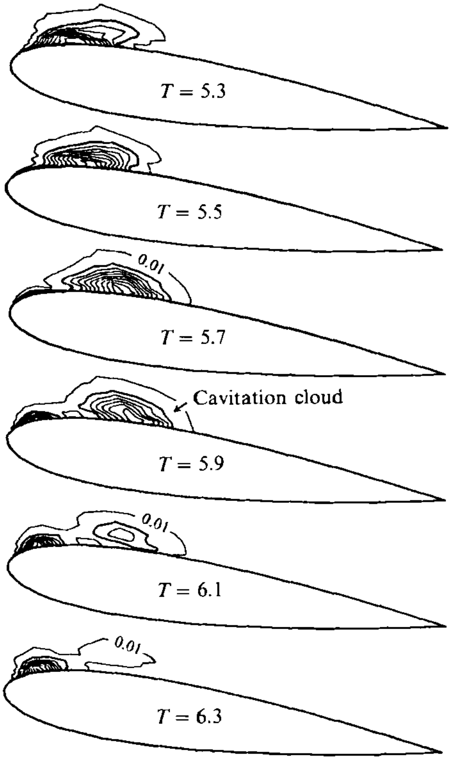

FIGURE 18. Void fraction contours around NACA0015 hydrofoil, $\sigma = 1.0$, $\alpha = 8°$, $Re = 3 \times 10^5$, the contour interval is 0.1 except for the most outer line.

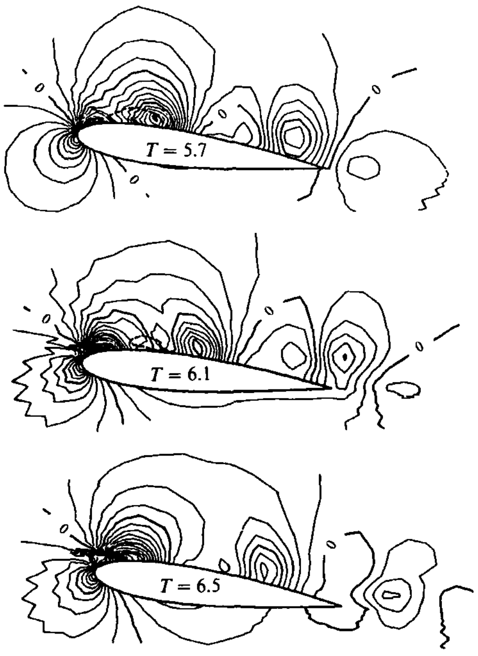

FIGURE 19. Pressure coefficient contours around NACA0015 hydrofoil, $\sigma = 1.0$, $\alpha = 8°$, $Re = 3 \times 10^5$, the contour interval is 0.1, the bold broken lines are void fraction contours of 0.1.

0.5832), the flow reattaches and the inflexion points exist in the velocity profiles. The measurement result downstream of a stable attached cavity shows similar inflexion points in the velocity profile (Yamaguchi *et al.* 1985; Kato, Yamaguchi & Kubota 1987). As shown in this figure, the generation of a cavity causes an increase in the boundary-layer thickness behind it. Figure 17 shows the comparison of the chordwise distributions of the boundary-layer-displacement thickness including the density effects for cavitating and non-cavitating conditions. For cavitating conditions, the displacement thickness decreases at the cavity collapsing region. It reaches a minimum at the mid-chord, then it begins to increase again. This is the same tendency as the experimental results (Kato *et al.* 1987).

4.3. *Mechanism of cloud cavitation*

Figure 18 shows void fraction contour lines at $\sigma = 1.0$ with the time increment of 0.2. For this condition, the unsteady cavity repeats growth and collapse. The highly distorted attached cavity sheds the cavitation cloud cyclically ($T = 5.9$). Then it soon collapses. This phenomenon agrees well with many experimental observations (Kermeen 1956; Wade & Acosta 1966; Alexander 1974; Shen & Peterson 1978; Izumida *et al.* 1980; Franc & Michel 1985).

Figure 19 shows pressure coefficient contours around the foil. Overlaid bold broken lines are void fraction contours of 0.1. As mentioned before, they show instantaneous cavity shapes. The negative pressure peaks correspond to the clockwise (positive) vortices (Kubota *et al.* 1989*b*). It is concluded consequently that the unsteady attached cavity sheds not only cavitation clouds but also vortices. The experimental result has confirmed such vortex-shedding phenomena (Kubota *et al.* 1989*a*).

Figure 20 shows close-ups of the velocity vectors around the cavity. This figure suggests the mechanism of the cavitation cloud shedding. At $T = 5.5$, a new separation vortex occurs at the cavity leading edge. A high velocity flow begins to

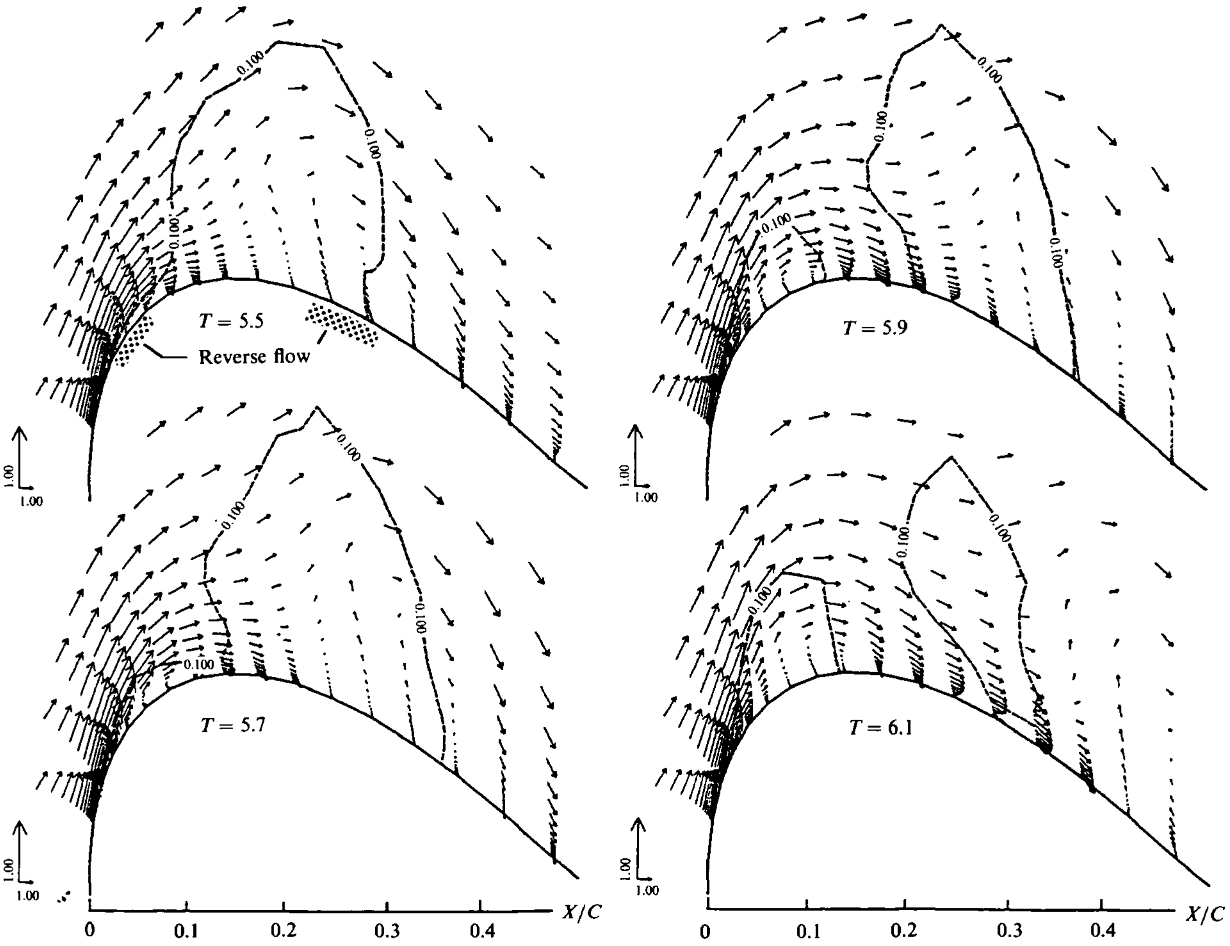

FIGURE 20. Close-ups of velocity vectors around NACA0015 hydrofoil, $\sigma = 1.0$, $\alpha = 8°$, $Re = 3 \times 10^5$, the bold broken lines are void fraction contours of 0.1. Vertical exaggeration of 4 : 1.

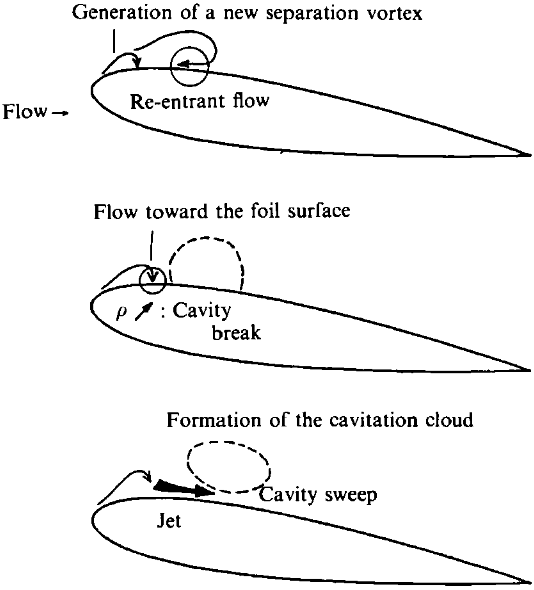

FIGURE 21. Mechanism of cloud cavitation.

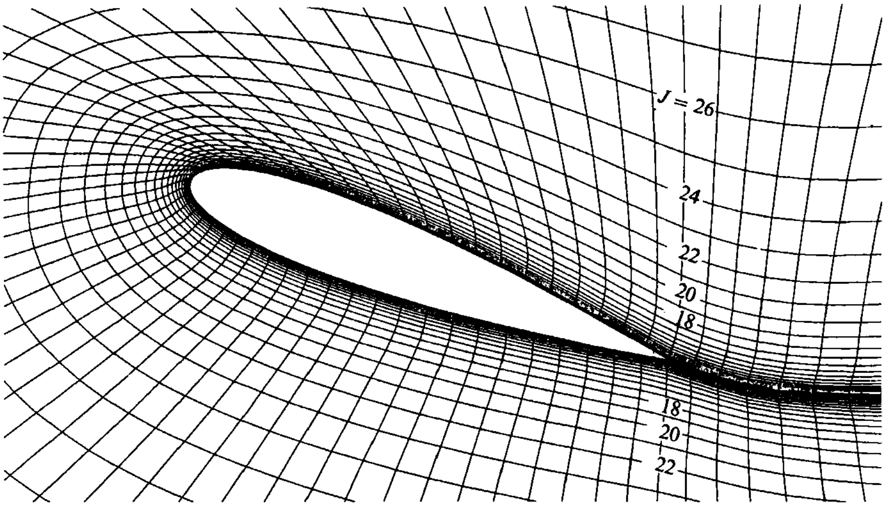

FIGURE 22. Close-up of the grid system around NACA0015 hydrofoil, $\alpha = 20°$, $101 \times 31 \times 3$.

appear near the wall region at the middle of the cavitation. Then the separation vortex induces the flow toward the foil surface ($T = 5.7$). Fluid density and pressure on the foil surface increase, owing to the impinging flow. It causes the cavity to break and tear off ($T = 5.9$, separation of the cavitation cloud). The impinging flow turns into the jet along the foil surface. The jet sweeps away the cavitation cloud ($T = 6.1$).

Figure 21 schematically illustrates the above mechanism of cloud cavitation. The most essential phenomenon seems to be the behaviour of the shear layer separated at the cavity leading edge. This is because it allows the jet into the cavity. The jet plays an important role in cavity break-offs. In other words, the unsteadiness of the shear layer produces the cavitation cloud. Another important point is the role of the re-entrant flow at the cavity trailing edge. Referring to the velocity vectors at

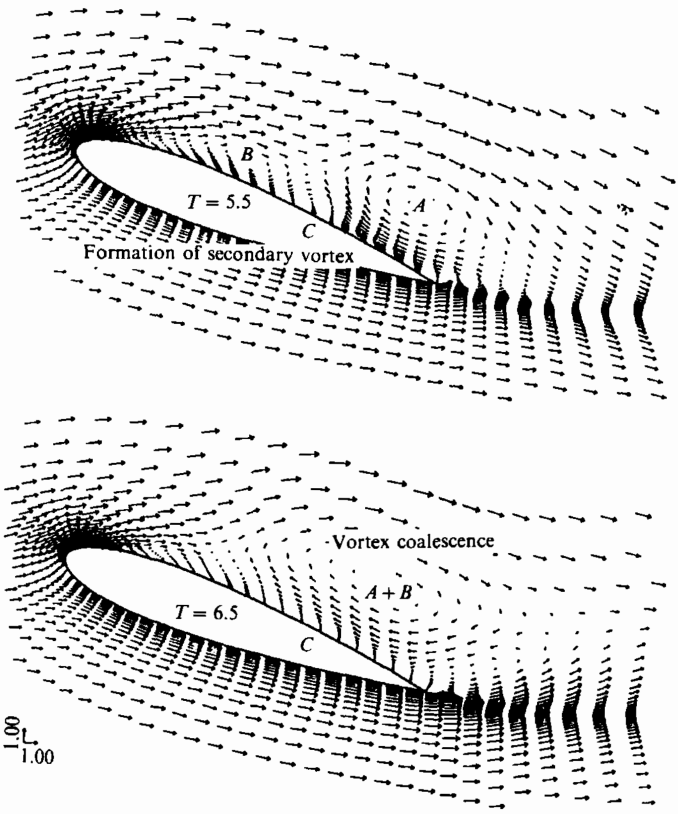

FIGURE 23. Velocity vectors around NACA0015 hydrofoil for non-cavitating conditions, $\alpha = 20°$, $Re = 3 \times 10^5$.

$T = 5.5$ in figure 20, we also observe reverse flow at the cavity trailing-edge region. This is what is called the re-entrant jet, which is observed by many researchers (Knapp *et al.* 1970). It is often said that the re-entrant jet progressing under the cavity towards the leading edge causes the cavity break-offs (Joussellin *et al.* 1991). However, as far as the present calculation is concerned, the wall jet seems to play a more important role in the separation mechanism of the cavitation cloud.

To examine the effect of the number of grid points, we performed the computation using a finer grid system at $\sigma = 1.0$. The number of grid points was $141 \times 41 \times 3$. The computational result shows the same tendency as the previous ones. We also observed the jet inside the cavity. The results show that the number of grid points has a lesser effect on the computed cavity appearances.

4.4. *Vortex cavitation around a hydrofoil at high angle of attack*

Next, we show the results around NACA0015 hydrofoil at an angle of attack α of 20°. The number of computational grid points was $101 \times 31 \times 3$. It was same as that at $\alpha = 0°$ and 8°. Figure 22 shows the close-up of the grid system. To resolve the fully separated large-scale vortices, grid points were not as concentrated near the foil surface. The minimum spacing was 6.20×10^{-3} at the trailing edge. It was about 7 times as wide as that at $\alpha = 8°$.

First, the onset of separation and the growth of the large-scale separation vortices are explained for non-cavitating conditions. At $\alpha = 20°$, large-scale separation vortices occur even for non-cavitating conditions.

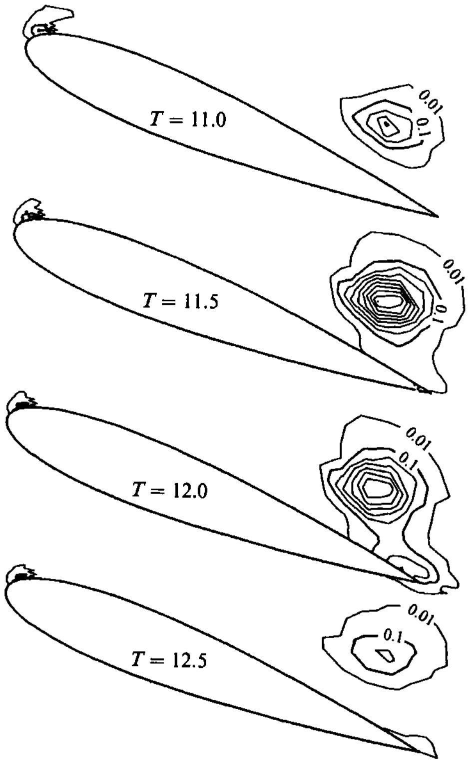

FIGURE 24. Void fraction contours around NACA0015 hydrofoil in the low-bubble-density condition (case *A*), $\sigma = 1.0$, $\alpha = 20°$, $Re = 3 \times 10^6$, the contour interval is 0.1 except for the most outer line.

Figure 23 shows the unsteady velocity vector fields around the hydrofoil. The first large-scale separation vortex *A* (clockwise) occurs at the leading edge and grows. Strong reverse flow is observed on the back. The vortex extends with time. At $T = 5.5$, the first separation vortex *A* stagnates above the trailing edge. A new separation vortex *B* appears and a secondary vortex *C* (counterclockwise) is formed between *A* and *B*. The secondary vortex *C* grows. Then, it extends below the first separation vortex *A*. A large reverse flow region appears between the foil surface and the first and the second separation vortices. The flow does not impinge on the foil surface. Since the first separation vortex *A* stays above the trailing edge, the separation vortex *B* continues to approach the vortex *A*. Finally, they coalesce at $T = 6.5$.

The above is the unsteady flow structure around a hydrofoil at high angle of attack for non-cavitating conditions. The separated shear layer from the leading edge rolls up first. Then, it turns into a large-scale vortex. The large-scale vortices repeat the cyclic procedures, i.e. formation – coalescence – shedding. This mechanism is deeply connected with the behaviour of the secondary vortices (Mehta & Lavan 1975). This secondary vortex is caused by the interaction between the separation vortices and the foil surface. The present grid system cannot fully resolve the small-scale vortex structure. However, it appears that the essential large-scale flow structure was resolved satisfactorily.

Johnsson (1969) showed experimentally that initial bubble number density affects

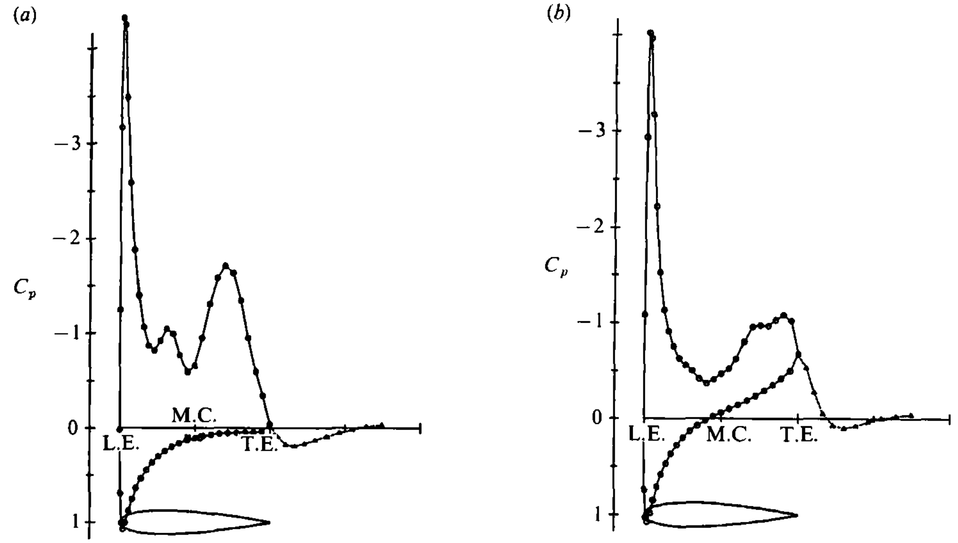

FIGURE 25. Comparison of pressure coefficient distributions, $\alpha = 20°$, $Re = 3 \times 10^5$. (a) $T = 10$, no cavitation. (b) $T = 11$, $\sigma = 1.0$ (case A).

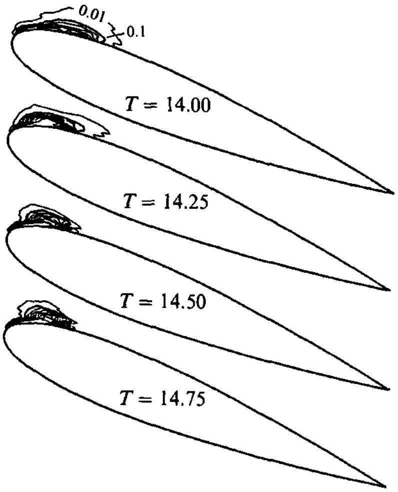

FIGURE 26. Void fraction contours around NACA0015 hydrofoil in the high-bubble-density condition (case B), $\sigma = 2.0$, $\alpha = 20°$, $Re = 3 \times 10^5$, the contour interval is 0.1 except for the most outer line.

appearances of vortex cavitation very much. Therefore, two different bubble-density conditions are adopted for the computation of a cavitating hydrofoil as follows:

	Density (n)	Initial radius (R_0)
Case A (lower density)	1×10^4	4×10^{-4}
Case B (higher density)	1×10^6	1×10^{-3}

The initial void fractions of case A and B are 2.68×10^{-6} and 4.19×10^{-3}, respectively.

Figure 24 shows the void fraction contour lines at $\sigma = 1.0$. The bubble number density is low (case A). For this condition, only large vortex cavitation occurs above the trailing edge. Only a small attached cavity occurs near the leading edge. The first

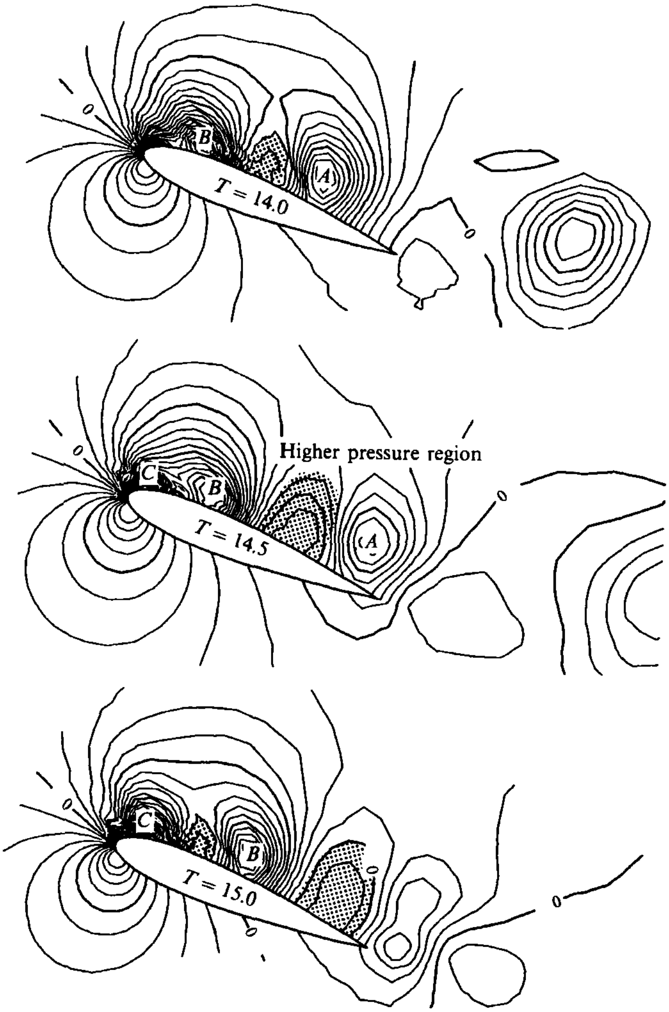

FIGURE 27. Pressure coefficient contours around NACA0015 hydrofoil in the high-bubble-density condition (case B), $\sigma = 2.0$, $\alpha = 20°$, $Re = 3 \times 10^5$, the contour interval is 0.1.

vortex cavitation appears at $T = 11$. It stagnates and grows as shown in this figure. At $t = 12$, this grown-up vortex cavity attaches to the foil surface. After that, it begins to disappear. The cavity hardly moves downstream during its whole life. The flow structure is similar with that for non-cavitating conditions even if the trailing-edge vortex cavitation occurs. The trailing-edge vortex cavitation disappears when the large-scale vortex is shed from the hydrofoil trailing-edge region.

Figure 25 shows the pressure distributions on the foil surface for non-cavitating and cavitating conditions ($\sigma = 1.0$, case A). Their shapes are almost the same. The peak at the leading edge remains, even for cavitating conditions. Though the pressure at this peak region is much lower than the vapour pressure ($C_p = -1$), no large attached cavity occurs there. This is because bubbles are too few and small to grow enough in such a short time.

Secondly, cavitation computations were performed under the higher-bubble-density condition (case B). Figure 26 shows the void fraction contours at $\sigma = 2$. Only unsteady attached cavity occurs near the leading edge. The attached cavity

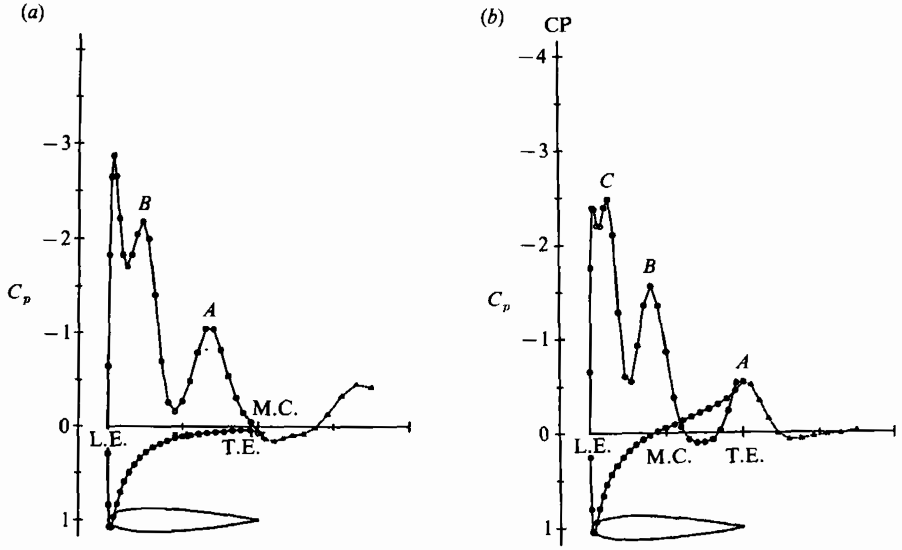

FIGURE 28. Instantaneous pressure coefficient distributions in the high bubble density condition (case B), $\sigma = 2.0$, $\alpha = 20°$, $Re = 3 \times 10^5$. (a) $T = 14.00$, $\sigma = 2.0$ (case B). (b) $T = 14.75$, $\sigma = 2.0$ (case B).

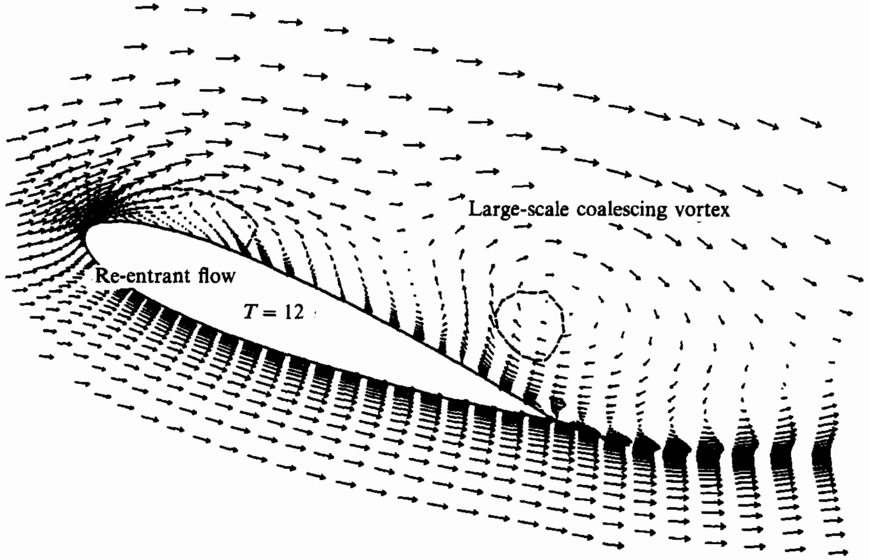

FIGURE 29. Veloity vectors around NACA0015 hydrofoil in the high-bubble-density condition (case B), $\sigma = 1.0$, $\alpha = 20°$, $Re = 3 \times 10^5$, $T = 12.0$, the bold broken lines are void fraction contours of 0.1.

oscillates at higher frequency than that at $\sigma = 1$ of case A (see figure 24). No vortex cavitation appears near the trailing edge. Under the lower-bubble-density condition (case A), a cavity did not appear at all for the same cavitation number of 2.

Figure 27 shows the pressure coefficient contours around the hydrofoil. At $T = 14$, the separated shear layer from the leading edge forms a large-scale vortex (lower pressure region; it is designated as A). This large-scale vortex does not stagnate above the trailing edge. This is because a higher pressure region remains between the two large-scale vortices. It pushes out the vortices smoothly as shown in this figure. As a result, vortices never coalesce there for the present condition ($T = 14.5$). After

		Leading-edge attached cavity	Trailing-edge vortex cavity	Vortex coalescence
No-cavitation		×	×	○
$\sigma = 2.0$	Case A	×	×	○
	Case B	○	×	×
$\sigma = 1.0$	Case A	×	○	○
	Case B	○	○	○

Case A: lower bubble density ($n = 1 \times 10^4, R_0 = 4 \times 10^{-4}$)
Case B: higher bubble density ($n = 1 \times 10^6, R_0 = 1 \times 10^{-3}$)

TABLE 2. Cavity types and vortex behaviour, NACA0015; $\alpha = 20°$; $Re = 3 \times 10^5$

the large-scale vortex has flowed out, a new separation vortex appears ($T = 15.0$). The most important feature of the flow structure is that no large reverse flow region appears on the back. The separated flow reattaches all the time. Accordingly, the flow always impinges between the large-scale vortices and causes the higher pressure region.

Figure 28 shows instantaneous pressure distributions on the foil surface. Small peaks correspond to respective roll-up vortices (see marks A, B, and C in figure 27). They move downstream with the vortices. The negative pressure peak near the leading edge is smaller than that for non-cavitating conditions, which has been shown in figure 29. This is because the attached cavity occurs there in case B.

Figure 29 shows the velocity vector fields around the hydrofoil under the higher-bubble-density condition (case B) at $\sigma = 1$. The bold broken lines are contours of $f_g = 0.1$ (cavity shapes). Both leading-edge attached cavity and trailing-edge vortex cavity are observed. Only the vortex cavity occurred under the lower-bubble-density condition at the same cavitation number (see figure 24). The leading-edge attached cavity is quite large at the higher-bubble-density condition. Nevertheless, it is rather stable, particularly at its front part. A very large-scale coalescing vortex is observed above the trailing edge. However, it is weaker than in case A. Strong reverse (re-entrant) flow exists at the end of the attached cavity all the time. It appears that the re-entrant flow scoops out the rear part of the attached cavity near the foil surface for these conditions.

As shown in the above calculation, the initial bubble radius and density have a great influence on the cavitating flow structure around a separated hydrofoil. Under the higher-bubble-density condition (case B), the attached cavity which occurs at the leading edge changes the structure of the separation vortices.

Lastly, table 2 shows an at-a-glance relationship chart between cavity types and vortex behaviour. All the computations in this study were carried out on the HITAC M-680H mainframe computer at the Computer Center of the University of Tokyo. The CPU time was about 1–20 hours.

5. Comparison with experimental results

5.1. *Experimental set-up and method*

To verify the aforementioned computational method and results with the program code SACT-III, experiments were performed for the same NACA0015 hydrofoil. Photographs and high-speed films of cavitation were taken for some typical conditions.

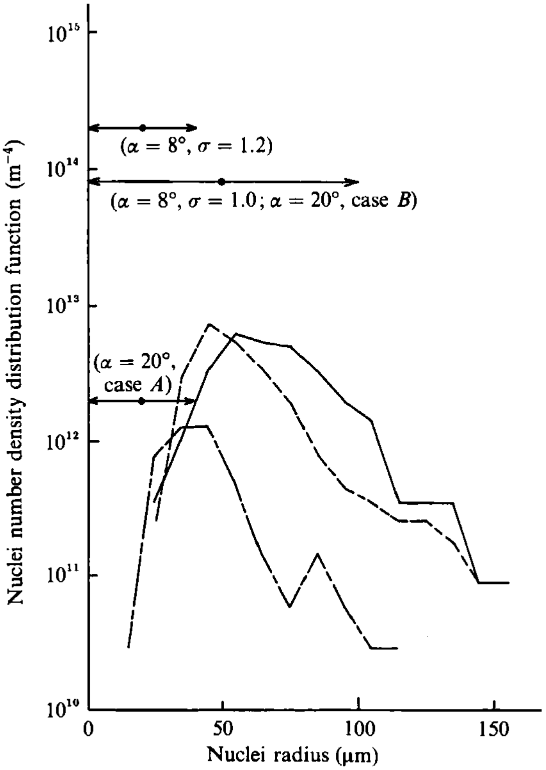

FIGURE 30. Comparison of nuclei number density distribution functions, α/α_s = 100% solid circles show those used for computations. ——, $\sigma = 1.20$; – – –, $\sigma = 2.30$; — — —, $\sigma = 3.54$.

All the experiments in this study were carried out in the Foil Test Section of the TE-type Cavitation Tunnel at the Department of Naval Architecture and Ocean Engineering, the University of Tokyo (Kodama *et al.* 1981; Inoue *et al.* 1986). The working section is 120 mm high and 50 mm wide. The turbulence level is low enough in the test section owing to the 6 wire-mesh screens placed upstream of the test section and the high contraction ratio (26:1). The measurement with an LDV showed that the turbulence level of the mean flow was about 0.3% on average. The velocity distribution measured with the LDV was uniform within 0.5%. The chord length and the span width of the hydrofoil NACA0015 model were 50 and 49 mm, respectively. The uniform velocity measurements were performed one-chord-length upstream of the foil section leading edge. The static pressure in the test section was measured with a strain gauge type pickup. The film speed of the 16 mm high-speed camera was about 4000 FPS. Uncertainty of the LDV (velocity) was about $+1\%$. The uncertainty of the pressure was $+1.5\times10^3$ Pa ($+0.015$ kg/cm^2).

The experiments were performed at angles of attack α of 8° and 20°. The Reynolds number Re was 3×10^5. They were the same as those for the computation. As a result, the uniform flow velocity was about 6 m/s since the water temperature was about 20 °C. To investigate the effects of bubble nuclei radius and density on cavitation, two conditions were chosen for the air content in the water. Those were 30 and 100% of the saturated condition at 1 atm. The air content was measured with a D. O. meter.

The number and size distributions of bubble nuclei in the water were measured in

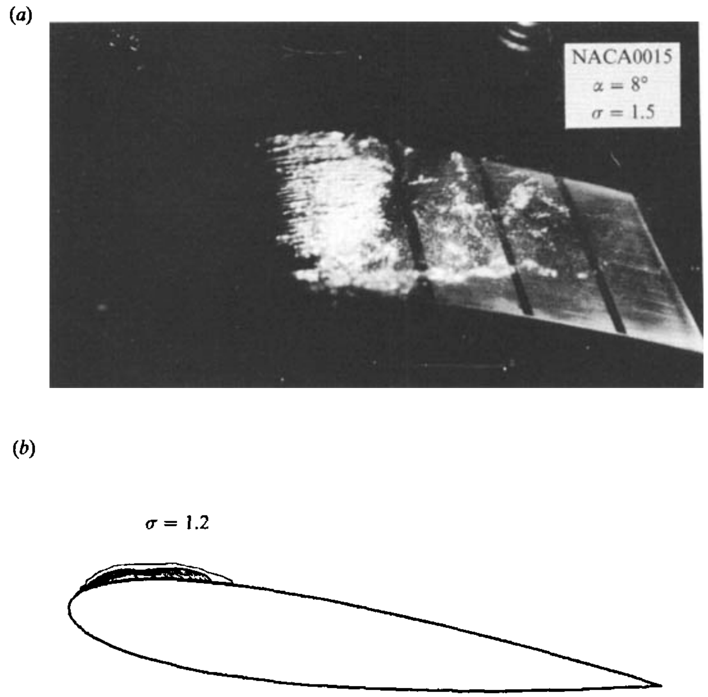

FIGURE 31. Comparison of sheet-type cavity appearance on NACA0015 hydrofoil, $\alpha = 8°$, $Re = 3 \times 10^5$, $\alpha/\alpha_s = 30\,\%$ (experiment). (*a*) Experimental observation. (*b*) Computed result.

		Bubble density n^* [m^{-3}]	Bubble radius R_0^* [µm]	Nuclei number density distribution [m^{-4}]
$\alpha = 8°$	$\sigma = 1.2$	8×10^9 $(n = 1 \times 10^6)$	20 $(R_0 = 4 \times 10^{-4})$	2×10^{14}
	$\sigma = 1.0$	8×10^9 $(n = 1 \times 10^6)$	50 $(R_0 = 4 \times 10^{-6})$	8×10^{13}
$\alpha = 20°$	Case *A*	8×10^7 $(n = 1 \times 10^4)$	20 $(R_0 = 4 \times 10^{-4})$	2×10^{12}
	Case *B*	8×10^9 $(n = 1 \times 10^6)$	50 $(R_0 = 4 \times 10^{-6})$	8×10^{13}

( ): non-dimensional value

TABLE 3. Dimensional bubble density and radius for computations, $d^* = 50 \times 10^3$ m

three cases using 35 mm photographs by a camera with telemicroscopic lenses. The area of the photographs was 8.76 mm × 6.51 mm. The depth of focus was estimated at 2.00 mm. The measurement point was same as that of the uniform flow velocity measurement. The air content in the water α/α_s was 100%. Figure 30 shows the measured nuclei number density distribution functions (Gates 1977). The bubble nuclei density increases with decreasing cavitation number, that is, with decreasing test section pressure, when the nuclei radius is more than 50 µm. Limitation of resolution of the photographs causes a reduction of the measured number of bubbles, especially those less than 50 µm radius. According to other measurements, the nuclei density increases monotonously with decreasing nuclei size. When the air content was 30%, no nuclei were observed in the photographs. Table 3 shows the

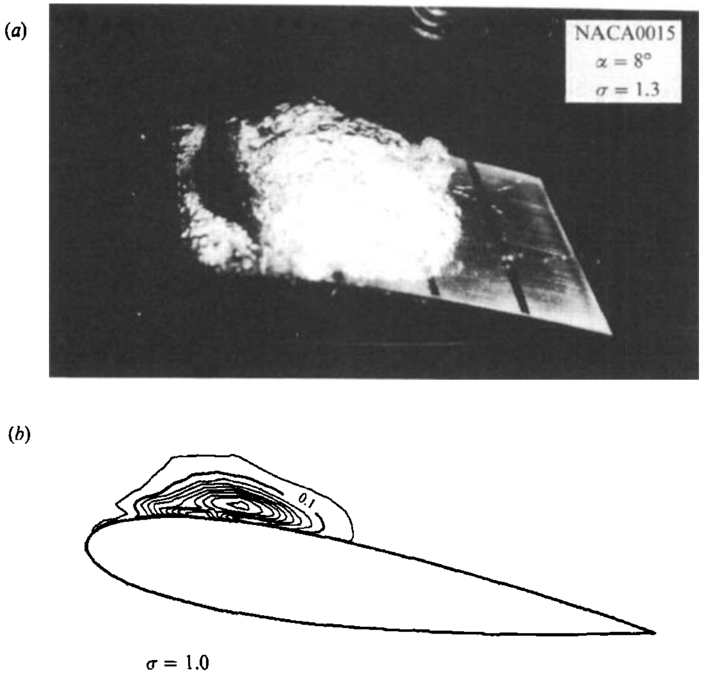

FIGURE 32. Comparison of cloud-type cavity appearance on NACA0015 hydrofoil, $\alpha = 8°$, $Re = 3 \times 10^5$, $\alpha/\alpha_s = 30\,\%$ (experiment). (a) Experimental observation. (b) Computed result.

dimensionalized initial bubble density and radius used for the computations (representative length $d^* = 50 \times 10^{-3}$ m). Furthermore, assuming that the radius of the bubble nuclei is distributed uniformly between 0 and $2R_0^*$, the nuclei number density distributions are obtained as shown in table 3. They are also illustrated in figure 30 with solid circles and arrows. Though the bubble nuclei may seem too many in the computations for $\alpha = 8°$, they are reasonable for the simulation of the cavity collapsing region. This is because the measurements with a light-scattering technique (Tamura *et al.* 1985) and a laser holography system (Maeda, Yamaguchi & Kato 1991) yielded a remarkable increase (more than 100 times) in bubble number behind an attached cavity.

5.2. *Cavitation appearance*

Figure 31 shows a photograph of cavitation at $\sigma = 1.5$. The angle of attack of the hydrofoil was 8°. The air content in the water was 30 %. We can observe the attached cavity followed by many small bubbles in the cavity collapsing region and the wake. Figure 31 also shows the computed cavity appearance at $\sigma = 1.2$. It agrees well with the experimental observation at $\sigma = 1.5$. The difference in the cavitation number (0.3) is almost equal to that of the pressure distributions for non-cavitating conditions between computed and experimental ones (see figure 11).

At the lower cavitation number, the whole cavity began to oscillate cyclically, even if the far-field condition was steady (Kubota *et al.* 1989*a*). Figure 32 shows a typical example of the cavity observation at $\sigma = 1.3$. As shown in this figure, the break-off of the attached cavity first occurs near the leading edge. The break-off point of the attached cavity agrees with the computational result. The separated cavitation cloud moves downstream with the attached part of the cavity growing. Then the cavitation cloud flows into the wake. Though the calculated cavitation cloud disappeared immediately (see figure 18), the experimentally observed

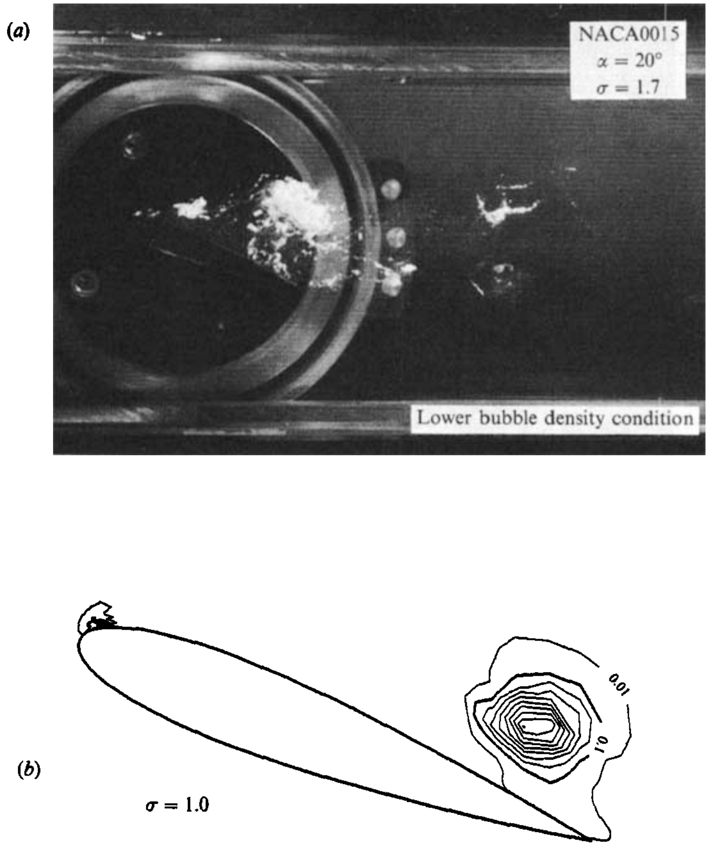

FIGURE 33. Comparison of vortex-type cavity appearance on NACA0015 hydrofoil in the low bubble density condition, $\alpha = 20°$, $Re = 3 \times 10^5$, $\alpha/\alpha_s = 30\,\%$ (experiment). (*a*) Experimental observation. (*b*) Computed result.

cavitation clouds remained for some time. This is because the present BTF model did not take into account the generation of the tiny bubbles at the cavity collapsing region and their concentration into the vortex centre. However, the difference between the model and the real phenomena appears not to much influence the fundamental mechanism of cavity break-off.

Next, appearance of cavitation is shown at an angle of attack of 20°. For non-cavitating conditions, a shear layer separates from the leading edge of the hydrofoil. It is composed of a succession of clockwise vortices. Figure 33 shows the side view of cavitation at $\sigma = 1.7$. The air content in the water was 30%. The cavitation inception occurs mainly in the separated flow region. Some bubble nuclei grow in the separated shear layer and expand explosively into large distorted cavities. Counterclockwise vortex cavitation also flows out of the foil trailing edge. No attached cavity occurs near the leading edge. While the cavitation number does not agree exactly, the computed cavity appearance at $\sigma = 1.0$ captures these features. The present microscopic cavity model used for the computation (LHM) is appropriate for the cavity growing in the separated flow region.

Figure 34 shows the cavity appearance at $\alpha/\alpha_s = 100\,\%$. The cavitation number was 2.3. The important feature is that the cavitation inception occurs near the leading edge of the hydrofoil as shown in this picture. In this case, the leading-edge cavity grows bigger with decreasing cavitation number. This leading-edge cavity is

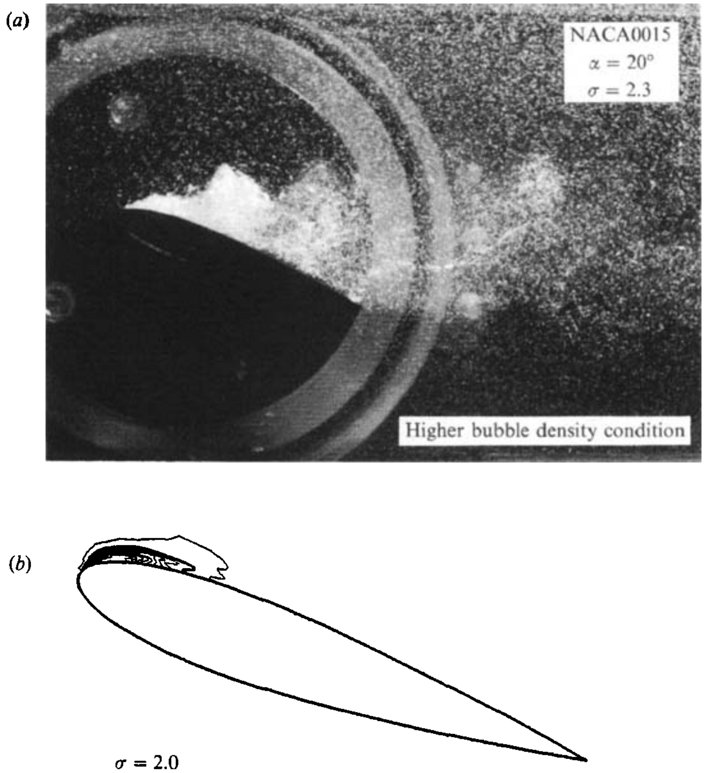

FIGURE 34. Comparison of vortex-type cavity appearance on NACA0015 hydrofoil in the high bubble density condition, $\alpha = 20°$, $Re = 3 \times 10^5$, $\alpha/\alpha_s = 100\%$ (experiment). (*a*) Experimental observation. (*b*) Computed result.

so unstable that the cavitation clouds are shed intermittently. Though there are many bubble nuclei in the wake region, no large vortex cavity occurs near the trailing edge of the hydrofoil.

The cavity appearance in figure 34 is quite different from that in figure 33. This is a typical example of the effect of bubble nuclei density on the cavity appearance. The computational result at $\sigma = 2.0$ captures and explains this phenomenon. Under the lower-bubble-density condition ($\alpha/\alpha_s = 30\%$ or case A, figure 33), no leading-edge cavitation occurs, since there are too few bubbles and too little time to grow the very small nuclei there. Accordingly, the behaviour of the separated free shear layer is similar to that for non-cavitating conditions. Separation vortices coalesce near the foil trailing edge and a large vortex cavitation appears there. On the contrary, cavity inception occurs near the leading edge of the hydrofoil at $\alpha/\alpha_s = 100\%$. This is because many large nuclei grow explosively in the low-pressure region of short duration at the foil leading edge. This leading-edge cavity changes the flow structure since it splits up the separation vortices. The rolling-up vortices flow out without coalescing near the trailing edge as shown in the computational result (see figure 27). As a result, no large-scale vortex cavitation occurs there.

5.3. *Vortex coalescence*

Figure 35 shows high-speed photographs of the cavitation appearance at an angle of attack of 20°. Cavitation number was 1.7 and the air content ratio was 30%. A time-interval between the respective pictures is 1.3×10^{-3} s (the non-dimensional time-

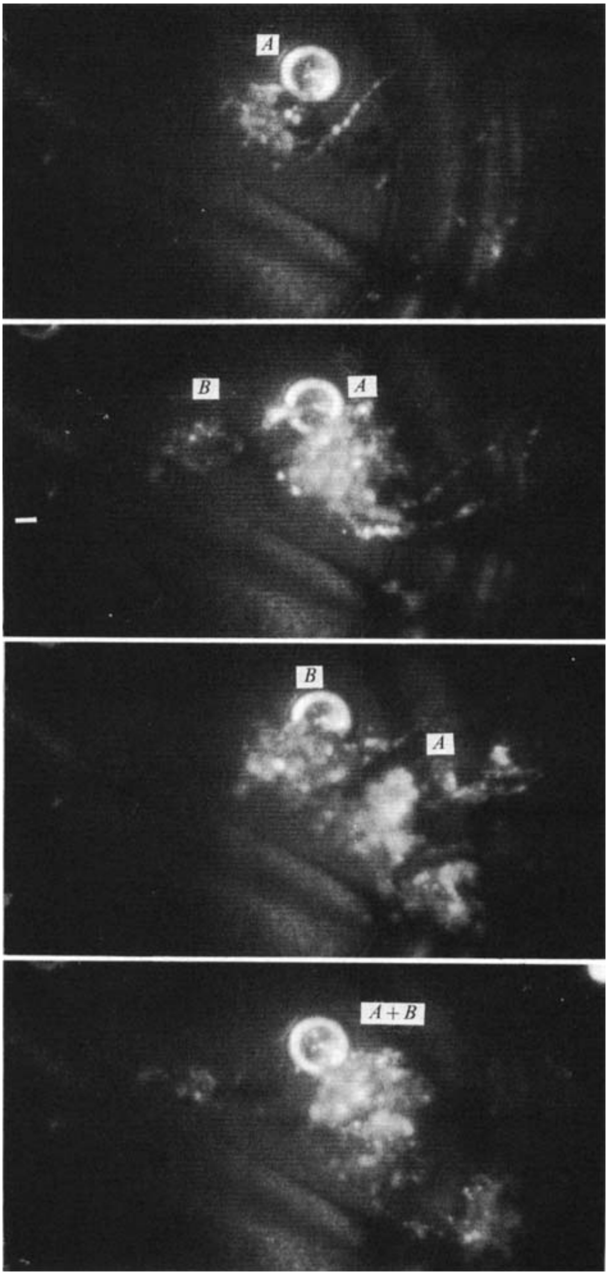

FIGURE 35. High-speed photographs of cavitation on NACA0015 hydrofoil, $\sigma = 1.7$, $\alpha = 20^\circ$, $Re = 3\times 10^4$, $\alpha/\alpha_s = 30\,\%$.

interval of 0.12). The coalescence of vortex cavitation is observed clearly in these pictures. The first vortex cavity A appears and grows above the trailing edge of the hydrofoil. It moves downstream very slowly. Next, the vortex cavity B appears and as it grows approaches the former vortex cavity A. The vortex cavity A hardly changes its position. As a consequence, the two vortex cavities A and B coalesce. Then, the coalescing vortex cavity $A+B$ flows downstream rapidly as it collapses. This vortex coalescing process has the same nature as the computed results.

6. Concluding remarks

In this study, the authors presented a new modelling concept of cavitation called a BTF (bubble two-phase flow) model. In a macroscopic view, this new cavity model treats the inside and outside of a cavity as one continuum. That is, it regards the cavity flow field phenomenologically as a compressible viscous fluid whose density varies greatly. Contour lines of void fraction can express the cavity shape. In a microscopic view, a simple LHM (local homogeneous model) is introduced. This is a kind of mean field approximation. This structural microscopic model treats a cavity as a locally homogeneous bubble cluster. Assuming bubble density and a typical bubble radius, a local void fraction function is given. The BTF cavity model is significant in the following points:

1. The BTF cavity model can investigate the nonlinear interaction between viscous flow with large-scale vortices and cavitation bubbles,
2. The BTF cavity model can consider the effects of bubble nuclei on cavitation inception and development,
3. The BTF cavity model can express unsteady characteristics of vortex cavitation.

The BTF cavity model, therefore, includes three essential factors for cavitation. Those factors are pressure, nuclei and time (Kato 1985). Furthermore, the BTF cavity model will be able to express the collapse of a bubble cluster by developing the model in future. By examining the computational and experimental results, the BTF cavity model has been proved useful for investigating vortex cavitation characteristics. Complicated interactions, in particular, between large-scale vortices caused by separation and bubble dynamics were clarified. However, further effort must be devoted to improvement of the microscopic cavity model. For instance, the pressure gradient of the vortex cavitation cloud might attract bubbles towards its centre. We must also take into account the convection and the distribution of bubbles, variation of the viscosity of the mixture and the slip between bubbles and liquid to predict the behaviour of cavitation clouds more accurately. Moreover, it is indispensable to clarify the effects of the grid spacing on the computed results and improve the computation scheme of SACT-III to obtain quantitative agreement with experimental results. The accuracy improvement of computational results is one of the most important subjects at present.

This research is partly supported by the Grant-in-Aid for Scientific Research of the Ministry of Education, Science and Culture. The authors express cordial thanks to Mr M. Maeda and Mr M. Miyanaga for their help. They also express their appreciation to Professor H. Ohtsubo for his encouragement and support.

REFERENCES

Abbott, I. H. & von Doenhoff, A. E. 1958 *Theory of Wing Sections*. Dover.

d'Agostino, L. & Brennen, C. E. 1989 Linearized dynamics of spherical bubble clouds. *J. Fluid Mech.* **199**, 155–176.

Alexander, A. J. 1974 Hydrofoil oscillation induced by cavitation. *Conf. on Cavitation, Edinburgh, IME, Herriot-Watt University*, 27–35.

Chahine, G. L. & Liu, H. L. 1985 A singular-perturbation theory of the growth of a bubble cluster in a superheated liquid. *J. Fluid Mech.* **156**, 257–279.

Efros, D. 1946 Hydrodynamics theory of two-dimensional flow with cavitation. *Dokl. Akad. Nauk. SSSR* **51**, 267–270.

Franc, J. P. & Michel, J. M. 1985 Attached cavitation and the boundary layer: experimental investigation and numerical treatment. *J. Fluid Mech.* **154**, 63–90.

Furness, R. A. & Hutton, S. P. 1975 Experimental and technical studies of two-dimensional fixed-type cavities. *Trans. ASME* I: *J. Fluids Engng* **97**, 515–522.

Furuya, O. 1975 Three-dimensional theory on supercavitating hydrofoils near a free surface. *J. Fluid Mech.* **71**, 339–359.

Furuya, O. 1980 Non-linear theory for partially cavitating cascade flows. *IAHR 10th Symp., Tokyo*, pp. 221–241.

Gates, E. M. 1977 The influence of freestream turbulence, freestream nuclei population and a drag-reduction polymer on cavitation inception on two axisymmetric bodies. PhD thesis, California Institute of Technology.

Harlow, F. H. & Welch, J. E. 1965 Numerical calculation of time-dependent viscous incompressible flow of fluid with free surface. *Phys. Fluids* **8**, 2182.

Helmholtz, H. 1868 On discontinuous movements of fluids. *Phil. Mag.* **36** (4), 337–346.

Hess, J. L. & Smith, A. M. O. 1967 Calculation of potential flow about arbitrary bodies. *Progress in Aeronautical Science*, vol. 8. Pergamon.

van Houten, R. J. 1982 The numerical prediction of unsteady sheet cavitation on high aspect ratio hydrofoils. *14th Symp. on Naval Hydrodyn. University of Michigan*, Session V, pp. 109–158.

Hutton, S. P. 1986 Studies of cavitation erosion and its relation to cavitating flow patterns. *Proc. Intl Symp. on Cavitation*, Sendai, Japan, vol. 1, pp. 21–29.

Inoue, S., Kato, H. & Yamaguchi, H. 1986 The effect of a slat on boundary layer characteristics and cavitation of the main foil. *Naval Arch. Ocean Engng*, **24**, 27–38.

Izumida, Y., Tamiya, S., Kato, H. & Yamaguchi, H. 1980 The relationship between characteristics of partial cavitation and flow separation. *Proc. 10th IAHR Symp., Tokyo*, pp. 169–181.

Johnsson, C. A. 1969 Cavitation inception on head forms, further tests. *Proc. 12th Intl Towing Tank Conf., Rome*, 381–392.

Jousselin, F., Delannoy, Y., Sauvage-Boutar, E. & Goirand, B. 1991 Experimental investigation on unsteady attached cavities. *Cavitation '91, ASME*, FED-116, pp. 61–66.

Kato, H. 1985 On the structure of cavity – new insight into the cavity flow: a summary of the keynote speech. *Intl Symp. Jets and Cavities, ASME*, FED-31, pp. 13–19.

Kato, H., Yamaguchi, H. & Kubota, A. 1987 Laser Doppler velocimeter measurements in cavitation tunnel. *Proc. 18th ITTC, Kobe*, vol. 2, pp. 433–437.

Kawamura, T. & Kuwahara, K. 1984 Computation of high Reynolds number flow around a circular cylinder with surface roughness. *AIAA papr* 84-0341.

Kermeen, R. W. 1956 Water tunnel test of NACA 4412 and Walchner profile 7 hydrofoil in non-cavitating and cavitating flows. Hydrodynamic Laboratory, California Institute of Technology, Pasadena, California, Rep. no. 47-5.

Kirchhoff, G. 1869 Zur Theorie Freier Flussigkeitsstrahlen. *J. reine angew. Math.* **70**, 289–298.

Kiya, M. & Sasaki, K. 1985 Structure of large-scale vortices and unsteady reverse flow in the reattaching zone of a turbulent separation bubble. *J. Fluid Mech.* **154**, 463–491.

Knapp, R. T., Daily, J. W. & Hammit, F. G. 1970 *Cavitation*. McGraw-Hill.

Kodama, Y. 1988 Three-dimensional grid generation around a ship hull using the geometrical method. *J. Soc. Naval Arch. Japan* **164**, 1–8.

Kodama, Y., Take, N., Tamiya, S. & Kato, H. 1981 The effect of nuclei on the inception of bubble and sheet cavitation on axisymmetric bodies. *Trans. ASME* I: *J. Fluids Engng* **103**, 557–563.

Kreisel, G. 1946 Cavitation with finite cavitation numbers. *Admiralty Res. Lab. Rep.* no. R1/H/36, p. 289.

Kubota, A., Kato, H. & Yamaguchi, H. 1988 A new numerical simulation method of cavitating flow caused by large-scale vortices. *Theoret. Appl. Mech., Tokyo* **36**, 93–100.

Kubota, A., Kato, H., Yamaguchi, H. & Maeda, M. 1989*a* Unsteady strcuture measurement of cloud cavitation on a foil section using conditional sampling technique. *Trans. ASME* I: *J. Fluids Engng* **111**, 204–210.

KUBOTA, A., KATO, H. & YAMAGUCHI, H. 1989*b* Finite difference analysis of unsteady cavitation on a two-dimensional hydrofoil. *5th Intl Conf. Numerical Ship Hydrodyn., Hiroshima*, pp. 472–487.

LAMB, H. 1932 *Hydrodynamics*. Dover. 112 pp.

LEMONNIER, H. & ROWE, A. 1988 Another approach in modelling cavitating flows. *J. Fluid Mech.* **195**, 557–580.

MAEDA, M., YAMAGUCHI, H. & KATO, H. 1991 Laser holography measurement of bubble population in cavitation cloud on a foil section. *Cavitation '91, ASME*, FED-116, pp. 67–75.

MEHTA, U. B. & LAVAN, Z. 1975 Starting vortex, separation bubbles and stall: a numerical study of laminar unsteady flow around an airfoil. *J. Fluid Mech.* **67**, 227–256.

MØRCH, K. A. 1981 Cavity cluster dynamics and cavitation erosion. *Cavitation and Polyphase Flow Forum – 1981*, pp. 1–10.

NISHIYAMA, T. & MIYAMOTO, M. 1969 Lifting-surface method for calculating the hydrodynamic characteristics of supercavitating hydrofoil operating near the free water surface. *Tech. Rep. Tohoku University* **34**, 123–139.

RIABOUCHINSKY, D. 1920 On steady fluid motion with free surface. *Proc. Lond. Math. Soc.* 2, **19**, 206.

ROACHE, P. J. 1976 *Computational Fluid Dynamics*. Albuquerque: Hermosa.

SHEN, Y. T. & PETERSON, F. B. 1978 Unsteady cavitation on an unsteady hydrofoil. *12th Symp. Naval Hydrodyn., Washington DC*, pp. 470–493.

SMAGORINSKY, J. 1963 General circulation experiments with the primitive equations – I. The basic experiment. *Mon. Weather Rev.* **91**, 99–164.

SOETRISNO, M., EBERHARDT, S., RILEY, J. J. & MCMURTRY, P. 1988 A study of inviscid, supersonic mixing layers using a second-order TVD scheme. *Proc. of AIAA/ASME/SIAM/APS 1st Natl Fluid Dyn. Congress, Cincinnati, Ohio*, pp. 1087–1094.

TAMURA, K., KATO, H., YAMAGUCHI, H., KOMURA, T., MAEDA, M. & MIYANAGA, M. 1985 Measurement of bubble nuclei by a scattered light technique. *Laser Doppler Velocimetry and Hot Wire/Film Anemometry*, Association for the Study of Flow Measurement, pp. 281–294.

TAYLOR, G. I. 1932 The viscosity of a fluid containing small drops of another fluid. *Proc. R. Soc. Lond.* **A**, **138**, 41–48.

THOMPSON, J. F., WARSI, Z. U. A. & MASTIN, C. W. 1985 *Numerical Grid Generation – Foundations and Applications*. Elsevier Science Publishing.

TULIN, M. P. 1955 Supercavitating flow past foils and struts. *Proc. NPL Symp. Cavitation Hydrodyn.* paper no. 16, pp. 1–19.

TULIN, M. P. 1964 Supercavitating flows – small perturbation theory. *J. Ship Res.* **7** (3), 16–37.

TULIN, T. P. & HSU, C. C. 1980 New applications of cavity flow theory. *13th Symp. Naval Hydrodyn., Tokyo, Shipbuilding Research Association of Japan*, pp. 107–131.

WADE, R. B. & ACOSTA, A. J. 1966 Experimental observation on the flow past a plano-convex hydrofoil. *Trans. ASME* I: *J. Fluids Engng* **88**, 273–283.

VAN WIJNGAARDEN, L. 1964 On the collective collapse of a large number of gas bubbles in water. *Proc. 11th Intl Cong. Appl. Mech.* pp. 854–861. Springer.

VAN WIJNGAARDEN, L. 1968 On the equations of motion for mixtures of liquid and gas bubbles. *J. Fluid Mech.* **33**, 465–474.

WU, T. Y. 1962 A wake model for free-stream flow theory. Part 1. Fully and partially developed wake flows and cavity flows past an oblique flat plate. *J. Fluid Mech.* **13**, pp. 161–181.

YAMAGUCHI, H. & KATO, H. 1982 A study on a supercavitating hydrofoil with rounded nose. *Naval Arch. Ocean Engng*, **20**, 51–60.

YAMAGUCHI, H. & KATO, H. 1983 On application of nonlinear cavity flow theory to thick foil sections. *Conf. on Cavitation, Edinburgh, IME*, pp. 167–174.

YAMAGUCHI, H., OSHIMA, A., KATO, H., KOMURA, T. & MAEDA, M. 1985 Measurement of the flow field downstream of a sheet type cavity. *Laser Doppler Velocimetry and Hot Wire/Film Anemometry*, Association for the Study of Flow Measurement, pp. 29–38.

YAMAGUCHI, H., KATO, H., SUGATANI, A., KAMIJO, A., HONDA, T. & MAEDA, M. 1988 Development of marine propellers with better cavitation performance – 3rd report: pressure distribution to stabilize cavitation. *J. Soc. Naval Arch. Japan* **164**, 28–42.